JGR Oceans

Key Points:

- Ice-tethered measurements in 2008, 2015, and 2017 in the Makarov Basin highlight changes in the upper and lower halocline properties
- The cold Atlantic-derived lower halocline progressed eastward along the East Siberian slope reaching the Chukchi Borderland
- The Makarov Basin lower halocline was increasingly supplied with warmer water resulting from the mixing of Atlantic water with shelf water

Correspondence to:
C. Bertosio and M. Athanase,
cecilia.bertosio.espci@gmail.com;
marylou.athanase@awi.de

Changes in Arctic Halocline Waters Along the East Siberian Slope and in the Makarov Basin From 2007 to 2020

Cécilia Bertosio[1] [iD], Christine Provost[1] [iD], Marylou Athanase[2] [iD], Nathalie Sennéchael[1] [iD], Gilles Garric[3] [iD], Jean-Michel Lellouche[3] [iD], Joo-Hong Kim[4] [iD], Kyoung-Ho Cho[4] [iD], and Taewook Park[4]

[1]LOCEAN-IPSL, Sorbonne Université (UPMC, University Paris 6), CNRS, IRD, MNHN, Paris, France, [2]Alfred-Wegener-Institut, Bremerhaven, Germany, [3]MERCATOR-OCEAN, Toulouse, France, [4]Korea Polar Research Institute, Incheon, Republic of Korea

Abstract The evolution of halocline waters in the Makarov Basin and along the East Siberian continental slope is examined by combining drifting platform observations, shipborne hydrographic data, and simulations from a global operational physical model from 2007 to 2020. From 2012 onwards, relatively shallow and cold Atlantic-derived lower halocline waters, previously restricted to the Lomonosov Ridge area, progressed eastward along the East Siberian continental slope. Their eastward extent abruptly shifted from 155°E to 170°E in early 2012, stabilized at 170°E until the end of 2015, then gradually advanced to reach the western Chukchi Sea in 2017. Such eastward progression led to a strengthening of the associated boundary current and to the shedding of mesoscale eddies of cold Atlantic-derived waters into the lower halocline of the Makarov Basin in September 2015 and near the East Siberian continental slope in November 2017. Additionally, active mixing between upwelled Atlantic Water and shelf water formed dense warm water supplying the Makarov Basin lower halocline. The increasing contribution from Atlantic-derived waters into the lower halocline along the East Siberian continental slope and in the Makarov Basin led to a weakening of the halocline, which is characteristic of a new Arctic Ocean regime that started in the early 2000s in the Eurasian Basin. Our results suggest that this new Arctic regime may now extend toward the Amerasian Basin.

Plain Language Summary In the Arctic Ocean, the "halocline" is a cold near-surface layer where salinity increases rapidly with depth. The halocline isolates the sea ice at the surface from the heat stored in the underlying warm and salty water. Hence, the strength of the halocline is a key feature in the maintenance of the sea ice cover. In this study, we use various ocean measurements and computer models to document recent changes in the halocline in the East-Amerasian sector of the Arctic. In this region, warm and salty water, usually found about a hundred meters deep, was found to become closer to the surface from 2012 onwards. We show that the shoaling of this warm water contributed to the progressive warming and weakening of the halocline in the East-Amerasian Arctic Ocean. This weakening of the halocline is emblematic of the emergence of a new Arctic regime, previously observed in the Eurasian sector of the Arctic, a region undergoing the growing influence from the Atlantic Ocean. Our study suggests the progression of this new regime, with shallow warm water and weakened halocline, further into the Arctic.

1. Introduction

In the cold Arctic Ocean, stratification is driven by salinity, in contrast with midlatitude oceans where stratification is driven by temperature (Carmack, 2007; Timmermans & Jayne, 2016). Consequently, the Arctic upper water column is composed of a fresh and cold surface mixed layer, separated from the underlying salty and warm Atlantic Water by a halocline layer. The Arctic Ocean halocline is about 100–200-m thick with large vertical salinity gradients, and insulates the sea ice at the surface from the heat carried by the underlying salty Atlantic Water layer (Carmack et al., 2016). Hence, the halocline is a key feature in the maintenance of the sea ice cover.

The strength of the halocline has been identified as an indicator of the ongoing Arctic changes. Since 1981, the halocline has strengthened in the Canada Basin and weakened in the Eurasian Basin (Bourgain & Gascard, 2011; Polyakov et al., 2018). In recent years, sea ice reduction, weaker stratification, and shoaling of the Atlantic Water layer in the Eurasian Basin led to deeper winter convection, which contributed to a weakening of the halocline (Athanase et al., 2020; Polyakov et al., 2017). These changes observed in the Eurasian Basin have

been referred to as the "Atlantification" of the Arctic Ocean and have accelerated over the past decade (Polyakov et al., 2017, 2020).

The structure and properties of the Arctic halocline layer differ from region to region, depending on the water mass composition and seasonal/local processes (Bourgain & Gascard, 2011, 2012). Freshened and cooled Atlantic Water found on the top of the Atlantic layer generally constitutes the lower halocline (LH) (e.g., blue layer in Figures 1c and 1d). This LH is relatively cold and shallow in the Eurasian Basin compared to that in the Canada Basin (∼−1.7 °C versus ∼−1 °C; McLaughlin et al., 2004; Timmermans et al., 2014). The transition zone between a cold and warm LH is believed to be located near the slope of the East Siberian shelf, although still little documented (Jung et al., 2021; Wang et al., 2021). Warmer LH water can result from diapycnal mixing between upwelled AW and bottom shelf waters, as well as enhanced vertical mixing of the LH with AW over sloped topography (Bauch et al., 2016; Fer et al., 2020; Schulz et al., 2021a; Wang et al., 2021; Woodgate et al., 2005). The upper halocline (UH; green layer in Figure 1d) receives relatively fresh and cold shelf waters—comprising river runoff and Pacific-origin waters—and exhibits different hydrographic/biogeochemical characteristics in the Eurasian, Makarov, or Canada Basins (e.g., Rudels et al., 2015; Swift et al., 1997).

The halocline of the Makarov Basin remains little documented, as the region is difficult to access for the deployment of drifting platforms or hydrographic surveys (Alkire et al., 2019; Morison et al., 1998). The UH of the Makarov Basin comprises advected shelf waters from the nearby Siberian or Chukchi seas where the large-scale surface Transpolar Drift (TPD, Figure 1a) current starts (e.g., Alkire et al., 2019; Steele & Boyd, 1998). The TPD transports water and sea ice across the Arctic toward Fram Strait and marks the front between Eurasian and Canadian water column structures (Morison et al., 1998, 2012). Before the 1990s, the TPD was located west of the Makarov Basin, above the Lomonosov Ridge (Morison et al., 1998), while trans-Arctic hydrographic sections post-1994 suggested that the TPD was located east of the Makarov Basin, over the Mendeleev Ridge (e.g., Carmack et al., 2016; Rainville & Winsor, 2008; Swift et al., 1997). The shifts in the TPD position respond to changes in atmospheric forcing and can influence the location where fresh shelf waters supply the UH of the Arctic Basins (Alkire et al., 2019; Steele & Boyd, 1998; Steele et al., 2004).

The halocline of the Makarov Basin can also be impacted by the Beaufort Gyre (BG), a large-scale surface circulation that dominates the nearby Canada Basin (Figure 1a). The BG constitutes the largest reservoir of freshwater in the Arctic (Haine et al., 2015; Proshutinsky et al., 2019). The halocline in the gyre is thick (∼250–300 m) and mainly comprises Pacific-derived waters from the Chukchi Sea (Proshutinsky et al., 2019; Shimada et al., 2005). After 2012, the BG extended westward over Mendeleev Ridge and reached the Makarov Basin (Bertosio et al., 2022; Regan et al., 2019). The impact of the extended BG on the water column in the Makarov Basin has been poorly documented so far.

In this study, we use in situ measurements and data from the 1/12° Mercator Ocean operational physical system PSY4 to investigate the evolution of the halocline in the Makarov Basin and along the East Siberian continental slope since 2007. We narrow down the location of the transition zone between the cold and warm LH along the East Siberian continental slope over the years and examine how the LH in the Makarov Basin is impacted. The paper is structured as follows. Data and methods are described in Section 2. Section 3 documents the progression of Atlantic-derived lower halocline waters along the slope over 2007–2020 from observations and numerical model output. In Section 4, we describe interannual variations of the upper and lower halocline in the western Makarov Basin. Section 5 summarizes our results and presents our conclusions.

2. Data and Methods

2.1. In Situ Measurements

We used data sets from autonomous ice-tethered platforms (ITP29, IAOOS15, and IAOOS25). Each Ice-Tethered Profilers (ITP) and Ice Atmosphere Ocean Observing System (IAOOS) platform consists of a surface system sitting atop an ice floe and an underwater profiler moving along a wire rope suspended from the surface element. Ocean profilers of the three platforms were equipped with a Seabird SBE41 Conductivity-Temperature-Depth (CTD) sensor measuring temperature and salinity beneath the sea ice as the platforms drift with the ice floe (Bertosio et al., 2021; Krishfield et al., 2008; Timmermans et al., 2010). Dissolved oxygen (DO) concentration was measured with a Seabird SBE43 sensor for the ITP29 and an Anderaa 4330 optical sensor for the two IAOOS
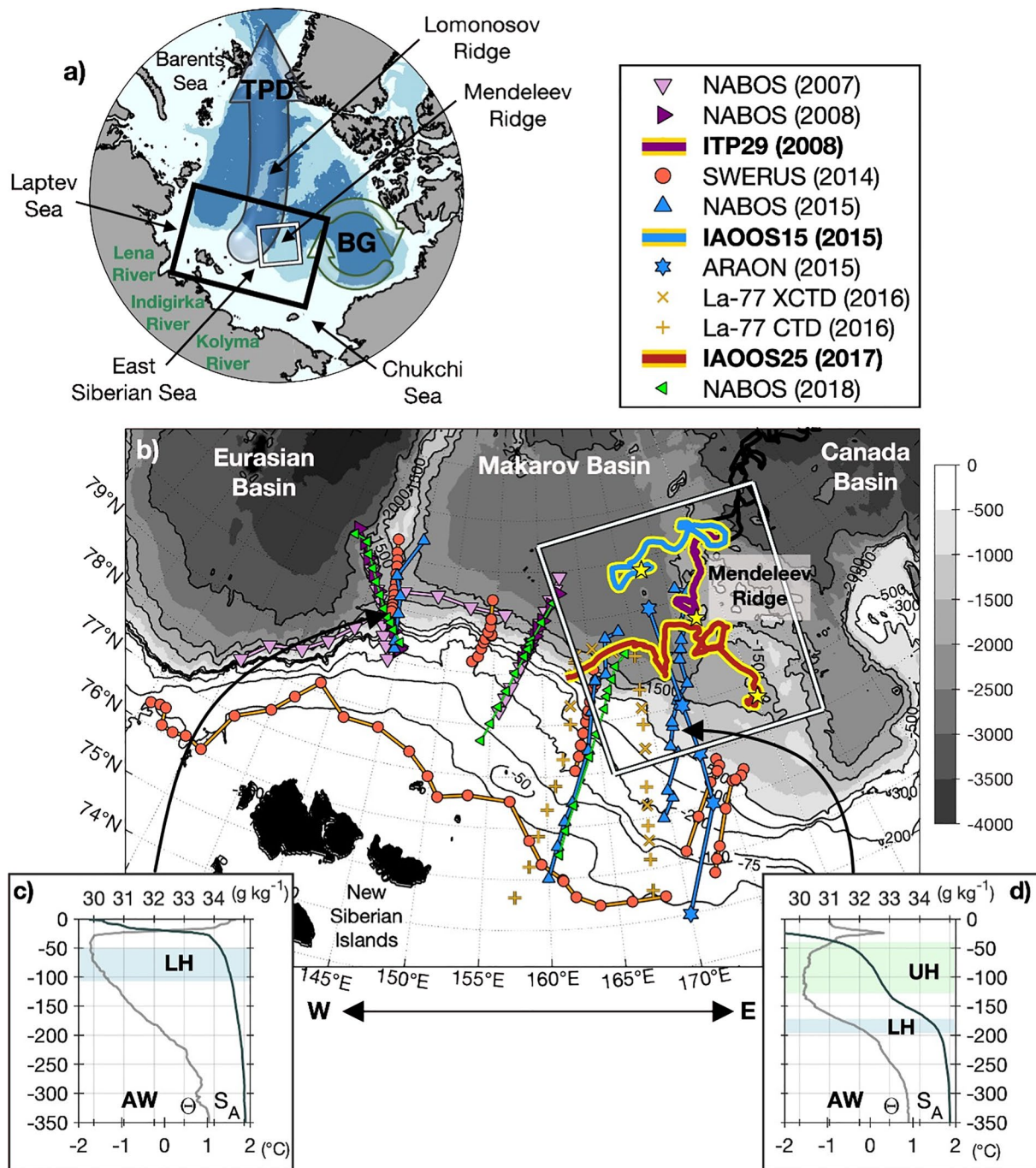
Figure 1. (a) Arctic bathymetry, the area under study is delimited by the black rectangle. Ocean floor shallower than 500 m is in light blue, between 500 and 2,500 m in medium blue, and larger than 2,500 m in dark blue. The Transpolar Drift (TPD) and the Beaufort Gyre (BG) are indicated by transparent arrows. (b) Shipborne CTD and drifting platforms data used in this study. The starting point of the drifting platforms ITP29, IAOOS15, and IAOOS25 is indicated by yellow stars. ITP trajectories are highlighted by the white box. IBCAO bathymetry is in grayscale. An "eastward shift" (resp. "westward shift") refers to a shift toward E (W) indicated below the lower panel. Two temperature (Θ; light gray) and salinity (S_A; dark gray) profiles are shown in (c) and (d), respectively (from NABOS, 2015). The location of each profile is shown by the black arrows. UH, Upper Halocline (green); LH, Lower Halocline (blue); AW, Atlantic Waters.

(Bertosio et al., 2021; Timmermans et al., 2010). We focused on the data obtained from the Makarov Basin to the Mendeleev Ridge (Figure 1b).

ITP29 was deployed on 31 August 2008 on the western flank of the Mendeleev Ridge (~79.5°N; 177°E, purple thick line in Figure 1b) and performed measurements in the ocean twice a day from 800 m up to 5 m (Krishfield

et al., 2008; Timmermans et al., 2010). The platform crossed the Mendeleev Ridge, the Makarov and Eurasian basins, and exited the Arctic through Fram Strait on 15 September 2010. We used the first 91 profiles which were located in the Makarov Basin (until 15 October 2008). IAOOS15 and IAOOS25 were deployed from the Korean Icebreaker R/V *Araon* during cruises in the northern Chukchi Sea (Bertosio et al., 2021). IAOOS15 was installed on 12 August 2015 in the Makarov Basin (80.8°N,173°E), about seven years after the ITP29 deployment. The IAOOS15 drifted across Mendeleev Ridge and the northern Canada Basin (blue thick line in Figure 1b). The platform provided temperature, salinity, and DO profiles until 30 October 2016. We focused on the first 80 profiles (i.e., until 15 October 2015), as they were located in the Makarov Basin and over Mendeleev Ridge. IAOOS25 was deployed on 15 August 2017 near southwest Mendeleev Ridge (77.7°N, 180°E) and drifted westward to the continental slope of the East Siberian Sea (ESS; red thick line in Figure 1b). IAOOS25 acquired temperature and salinity data until 19 November 2017 and lost the profiler over the East Siberian slope. IAOOS profilers were set to perform two upward profiles per day from 5 m down to 300 m (IAOOS15) and 430 m (IAOOS25). For calibration, the first profiles from IAOOS platforms were compared to the ship CTD profiles closest to the deployment site. After quality control, conservative temperature (Θ) and absolute salinity (S_A) have an accuracy of ±0.005 °C and ±0.02 g kg^{-1}, respectively. The data were interpolated to 0.5 m vertical resolution bins. Further description of the IAOOS experimental setup and data processing is given in Athanase et al. (2019) and Bertosio et al. (2021).

We used additional shipborne CTD measurements from expeditions including SWERUS (Swedish-Russian-US Arctic Ocean Investigation of Climate-Cryosphere-Carbon Interactions) in July-September 2014 (Anderson et al., 2017), the Nansen and Amundsen Basin Observation System (NABOS and NABOS-II; Lenn et al., 2009) program in September 2007, October 2008, September 2015, and September 2018, ARA06B expedition in August 2015 with the Korean Icebreaker R/V *Araon* (Jung et al., 2021), and the Russian campaign *La-77* in September 2016 (Wang et al., 2021; Figure 1).

2.2. Mercator Ocean Operational System

The global operational system PSY4 was developed at Mercator Ocean for the Copernicus Marine Environment Monitoring Service (CMEMS; http://marine.copernicus.eu/) and simulates physical ocean variables (e.g., temperature, salinity, sea surface height, and velocity) and sea ice variables from 2007 onwards (Lellouche et al., 2018). The physical configuration is based on a 1/12° tripolar grid (spacing of 3–5 km in the Arctic; Madec & Imbard, 1996), with 50 vertical levels of decreasing resolution (~1 m at the surface; ~100 m at 300-m depth), including 22 levels within the upper 100 m. The system PSY4 uses version 3.1 of the Nucleus for European Modelling of the Ocean model (NEMO; Madec et al., 2008) and the Louvain-La-Neuve thermodynamic-dynamic sea Ice Model (LIM2; Fichefet & Maqueda, 1997). At the surface, the model is driven by atmospheric analysis and forecasts obtained from the European Centre for Medium-Range Weather Forecasts-Integrated Forecast System (ECMWF-IFS; https://www.ecmwf.int/) at 3-hr resolution. Apart from sea ice concentrations obtained from OSI-SAF products (https://doi.org/10.48670/moi-00134), no assimilation is performed in the ice-covered ocean in the Arctic. Bertosio et al. (2022) found satisfactory skills in simulating sea ice cover, temperature, salinity, sea surface height, and ocean currents in the Arctic basin (see also Athanase et al., 2019, 2020; Koenig Provost, Sennéchael, et al., 2017 and Koenig, Provost, Villacieros-Robineau, et al., 2017). Further evaluation showed that PSY4 fields were very consistent with observations in the ESS and Makarov Basin (Figures S1 and S2 in Supporting Information S1).

2.3. Definition of Halocline Boundaries

In this study, we used density anomalies σ (kg m^{-3}), referred to as density hereafter. Absolute salinity S_A (g kg^{-1}) and conservative temperature Θ (°C) are used following the TEOS-10 (Thermodynamic Equations of Seawater) international standard (Feistel, 2018; McDougall & Barker, 2011).

The top of the halocline, i.e., the base of the mixed layer, was identified through visual inspection as the depth of the shallowest vertical salinity gradient maximum (e.g., Bourgain & Gascard, 2012; Rudels et al., 2000; Timmermans et al., 2012). These maxima corresponded, on average, to the 25 kg m^{-3} isopycnal (Figure 2a).

The UH of the Makarov Basin is composed of advected shelf waters from the East Siberian Sea (ESS) or the Chukchi Sea, which both comprise Pacific-origin waters (Anderson et al., 2011, 2017; Wang et al., 2021). We defined the UH as lying between isopycnals 25 and 26.4 kg m^{-3}, in agreement with the densities of waters encountered
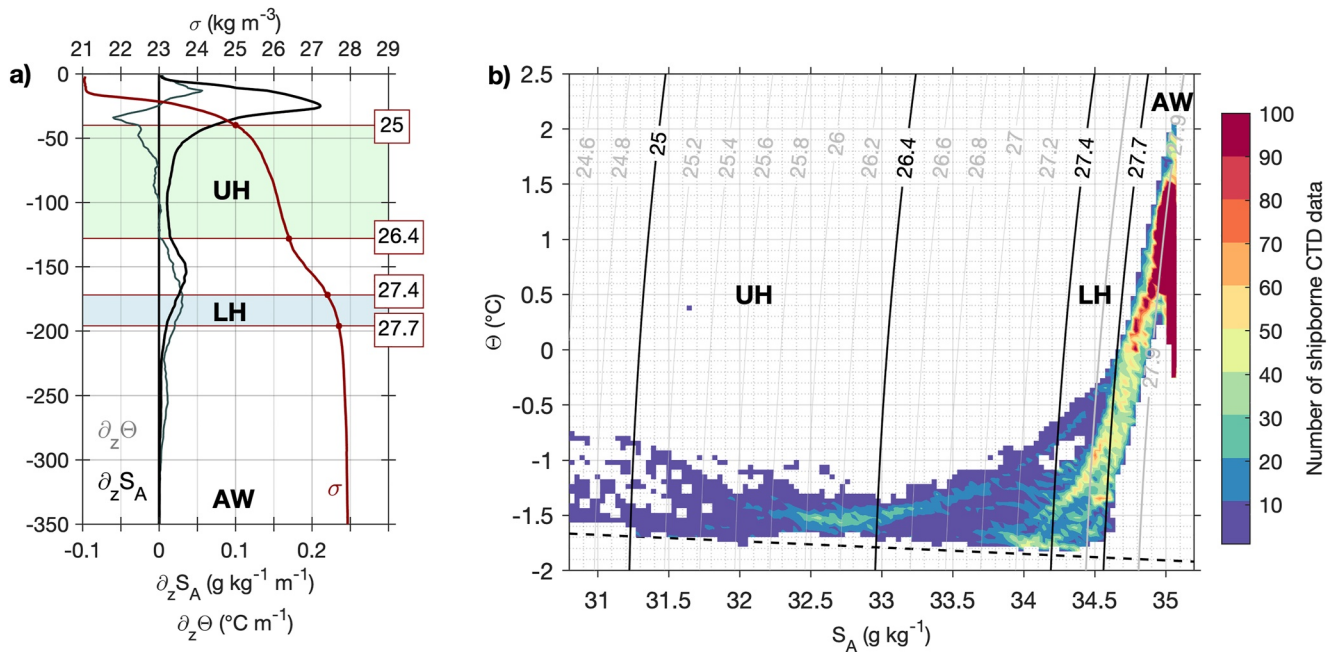
Figure 2. (a) Example of profiles of vertical gradients of salinity ($\partial_z S_A$ in black; g kg^{-1} m^{-1}; bottom x-axis), temperature ($\partial_z \Theta$ in gray; °C m^{-1}; bottom x-axis), and profiles of density (σ in red; kg m^{-3}; top x-axis). Data are from NABOS (2015) (same as in Figure 1d). The density limits of the layers (σ values in the red boxes) are indicated by horizontal red lines. (b) Θ-S_A diagram from shipborne CTD data shown in Figure 1. The number of data points is in color. UH, Upper Halocline (green); LH, Lower Halocline (blue); AW, Atlantic Waters.

in the ESS and Chukchi Sea (e.g., Pisareva et al., 2015; Wang et al., 2021). The base of the UH was marked by a temperature minimum of around 33–33.1 g kg^{-1}, which is consistent with the definition suggested by Steele and Boyd (1998). The UH was separated from the LH by a 50-m-thick layer associated with a secondary peak in the salinity vertical gradients (Figure 2a). The base of the LH was detected as a bend in the temperature-salinity curve, found on average between isopycnals 27.4 and 27.7 kg m^{-3} ($34.2 < S_A < 34.6$ g kg^{-1}; $-1.4 < \Theta < -0.6$ °C, Figure 2b). Atlantic Waters (AW, $S_A > 34.9$ g kg^{-1} and $\Theta > 0$ °C) were found below a large temperature gradient (the thermocline) and characterized by a local maximum in the temperature-salinity curve at denser values than 27.7 kg m^{-3} (Figure 2b).

Halocline vertical boundaries obtained from these density criteria were compared to those obtained from other criteria found in the literature. Bourgain and Gascard (2011) identified the base of the halocline using the constant density ratio value $R_\rho = \alpha \Delta \Theta / \beta \Delta S_A = 0.05$ with α, the thermal expansion coefficient, and β, the haline contraction coefficient. In our study, densities associated with $R_\rho = 0.05$ were between 27.3 and 27.75 kg m^{-3} which corresponded to the density interval we used for the LH. Alternatively, the base of the halocline defined as the depth of the value $S_A = 34.46$ g kg^{-1} ($S = 34.3$ psu) (Rudels et al., 1996) was, on average, 40 m shallower than isopycnal 27.7 kg m^{-3}. In Rudels et al. (1996), this salinity-based definition was applied to hydrographic profiles collected in 1980 and 1991. Recent observations in 2017 in the Western Eurasian Basin showed that water column properties changed and the base of the halocline was found closer to the 34.9 g kg^{-1} isohaline (Bertosio et al., 2020). In the rapidly changing Arctic Ocean, comparisons of isohaline-based and isopycnal-based criteria should thus be interpreted with caution.

2.4. Available Potential Energy

We used the available potential energy (APE) to quantify the strength of the halocline. The APE was computed as (e.g., Bertosio et al., 2020; Colin de Verdière et al., 2018; Polyakov et al., 2018)

$$APE = \int_{z_{27.85}}^{z=0} g(\sigma(z) - 27.85)z\,dz \tag{1}$$

where g is the gravitational constant and σ is the density anomaly. The depth $z_{27.85}$ is the depth of the isopycnal 27.85 kg m^{-3} and corresponds to the base of the halocline layer.

3. Progression of Atlantic-Derived Lower Halocline Waters Along the East Siberian Continental Slope Over 2007–2020

3.1. Lower Halocline Changes Along the East Siberian Continental Slope From Shipborne CTD

We documented the spatial and temporal changes of the LH using sections of shipborne CTD stations across the East Siberian continental slope (Figure 3). The 27.6 kg m^{-3} isopycnal marked the location of the LH and divided the area into four subregions: the Lomonosov Ridge, the west ESS (wESS), the central ESS (cESS), and the east ESS (eESS). Three distinct periods were considered: 2007–2008, with data at Lomonosov Ridge and wESS; 2014–2015, with data all along the continental slope; and 2016, with data at central and eESS. Major hydrographic properties are summarized in Table 1.

At the Lomonosov Ridge, the LH temperature was, on average, colder than −1.5 °C for all years, while salinity increased from $S_A \sim$ 34.2–34.3 g kg^{-1} in 2007–2008 to $S_A \sim$ 34.4–34.5 g kg^{-1} in 2014–2015 (Figures 3a–3d). This salinity increase, associated with sustained cold temperatures, likely resulted from changes upstream of the Lomonosov Ridge or from coastal polynya water influence (Anderson et al., 2017; Bauch & Cherniavskaia, 2018; Bertosio et al., 2020; Polyakov et al., 2020). At the Lomonosov Ridge, the LH was warmer over the continental slope than off-shore ($\Delta\Theta < 0.3$ °C), potentially resulting from enhanced vertical mixing with AW over sloping topography (Dmitrenko et al., 2011; Lenn et al., 2009; Schulz et al., 2021b) (green and dark red dots in Figures 3a–3d).

From wESS to cESS, the LH salinity varied little in time, while temperatures were always higher than those at the Lomonosov Ridge (−1.5 < Θ < −0.5 °C, Figures 3e–3j). Note that, in contrast, AW was colder along the East Siberian continental slope than at Lomonosov Ridge (Θ ~ 1 °C versus Θ > 1 °C). At cESS, the LH exhibited striking spatial temperature differences in 2014–2015 with waters over the continental slope warmer than off-shore ($\Delta\Theta \sim 1$ °C, black and dark red dots in Figures 3h and 3i), suggesting two different types of LH. In 2016, over the eESS continental shelf and slope, near the Chukchi Sea, a bend in the associated Θ-S$_A$ curves suggested the presence of Atlantic-derived LH that was absent in 2014 and 2015 (Figures 3k–3m).

3.2. Evolving Contributions of the Atlantic-Derived Lower Halocline Along the East Siberian Continental Slope

We used the model output to investigate the contributions of Atlantic-derived lower halocline waters to the lower halocline along the East Siberian continental slope. We considered the evolution of the temperature on the 27.6 kg m^{-3} isopycnal (in the LH) and APE from both in situ measurements and monthly mean PSY4 fields (Figures 4 and 5). Interannual changes were examined along the 300-m isobath (on the continental shelf) and the 1,000-m isobath (on the continental slope).

From 2007 to 2011, there was a marked temperature and APE front located between 155°E (on the shelf) and 160°E (on the slope) (Figures 4a, 4b, and 5). West of this front, the LH was colder than −0.6 °C and likely corresponded to cold Atlantic-derived LH from the Eurasian Basin. Low values of APE indicated a weak stratification (APE < 10 × 10^4 J m^{-2}, Figures 4b and 5d). In contrast, east of 160°E temperatures were higher than −0.4 °C with APE > 20 × 10^4 J m^{-2} (Figures 4a, 4b, and 5). The position of the front over the 2007–2011 period exhibited large seasonal variations, reaching its westernmost limits in fall/winter (Figure 5). The 27.6 kg m^{-3} isopycnal above the 1,000-m isobath was deeper in the east than in the west: this is consistent with a thicker UH resulting from shelf water influence in the east, and inducing a deeper LH (Figure 5c). The front shifted eastwards in winter 2011–2012, reaching 171°E above the 1,000-m isobath, and decreasing stratification over the continental slope (Figures 4d and 5d). The rapid eastward shift of Atlantic-derived LH along the continental slope in winter 2011–2012 occurred at a time of large easterly winds over the ESS (Figure S3b in Supporting Information S1), and relatively weak inflow through Bering Strait (Peralta-Ferriz & Woodgate, 2017; Serreze et al., 2019; Woodgate, 2018). From 2012 onwards, seasonal variations of the front were less pronounced. East of ~172°E, the APE increased in 2010–2011 (Figure 5d), which likely resulted from the BG influence in that period as suggested by Bertosio et al. (2022) and Regan et al. (2019). After winter 2015–2016, the front progressively
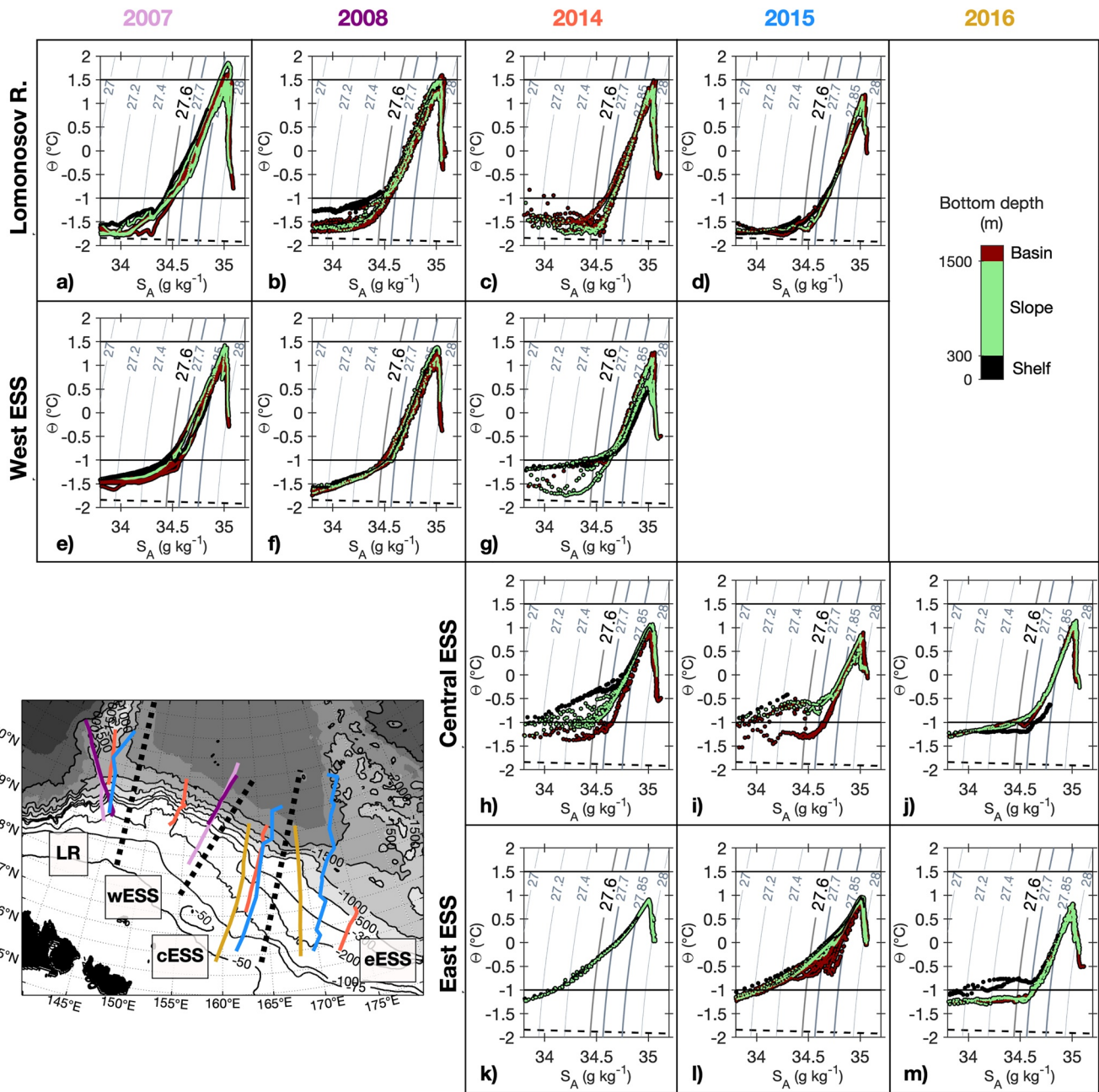
Figure 3. Θ-S_A diagrams from sections along the East Siberian Sea (y-axis in °C and x-axis in g kg^{-1}). Columns indicate years and rows correspond to the four areas delimited with dashed black lines on the map: the Lomonosov Ridge (LR) and the west, central and east East Siberian Sea (wESS, cESS, and eESS, respectively). Isopycnal 27.6 kg m^{-3} corresponds to a landmark for the LH. In Θ-S_A diagrams, color corresponds to bathymetry (in m) at each point. Colors of hydrographic sections on the map indicate the year (same color code as in Figure 1; 2007: light purple; 2008: purple; 2014: orange; 2015: blue; and 2016: yellow).

moved east until winter 2017. From then, warm LH waters (>−0.4 °C) were no longer found along the slope and the stratification was lower than 20×10^4 J m^{-2} (Figures 4e, 4f, and 5). The cold Atlantic-derived LH from the Lomonosov Ridge likely reached the western Chukchi Sea in winter 2017.

The along-slope eastward progression of cold Atlantic-derived LH was observed from shipborne CTD measurements (Figure 4). Drifting platform data also suggested an evolving contribution from the cold Atlantic-derived LH to the Makarov Basin LH, which is further investigated in the following section (Figure 4).

Table 1
Lower Halocline Mean Density (σ, kg m⁻³), Absolute Salinity (S_A, g kg⁻¹), and Conservative Temperature (Θ, °C) Over the East Siberian Shelf (Bathymetry <300 m), Slope (300–1,500-m Isobath), and in the Makarov Basin (Beyond 2,000m Isobath)

		2007–2008			2014–2015			2016		
		Shelf	Slope	Basin	Shelf	Slope	Basin	Shelf	Slope	Basin
Lomonosov ridge	σ	27.4	27.4	27.4	27.6	27.6	27.6			
	S_A	34.2	34.2	34.2	34.4	34.5	34.5			
	Θ	−1.3	−1.6	−1.7	−1.5	−1.5	−1.5			
West ESS	σ	27.5	27.5	27.6	27.7	27.7	27.7			
	S_A	34.3	34.3	34.4	34.6	34.6	34.6			
	Θ	−1.2	−1.2	−1.2	−0.9	−1.1	−1.1			
Central ESS	σ				27.7	27.6	27.7	27.7	27.6	27.7
	S_A				34.6	34.5	34.6	34.6	34.5	34.6
	Θ				−0.4	−0.7	−1.2	−1.2	−0.9	−1
East ESS	σ						∼27.7	27.7	27.7	27.7
	S_A						∼34.6	34.6	34.6	34.6
	Θ						∼−0.6	−0.8	−1.2	−1.2

Note. See Figure 3 for the locations. ESS, East Siberian Sea.

4. Interannual Variations in the Western Makarov Basin Halocline

For this section, we used measurements from the three drifting platforms in the late summer of 2008, 2015, and 2017 (Figures 6, 7, and 8), and monthly modeled fields of temperature, salinity, and horizontal velocity (Figures 9 and 10) to document the evolution of the upper and lower halocline in the Makarov Basin. In particular, we aimed to investigate the evolving contribution of Atlantic-derived waters from the continental slope to the open basin.

4.1. Upper Halocline: Varying Influence of Pacific Water

The UH ($25 < \sigma < 26.4$ kg m⁻³) showed distinct thicknesses in 2008, 2015, and 2017 (Figure 6 and Table 2). The UH was thicker in 2015 (∼110 m) compared to 2008 (∼70 m) and 2017 (∼40 m; Table 2). UH temperatures in 2008 and 2015 exhibited a local maximum (Θ_{max}) below the mixed layer at $S_A \sim 31.5$ g kg⁻¹ overlying a minimum Θ_{min} at $S_A \sim 32.6$–33 g kg⁻¹, with larger values in 2015 than in 2008 ($\Delta\Theta \sim 0.4$ °C, Table 2, Figures 7a and 7b). In 2015, the salinities associated with the Θ_{max} were consistent with the influence of Pacific summer waters (Shimada et al., 2001; Steele et al., 2004; Timmermans et al., 2014, 2017). The BG, inside which the UH is thick and largely influenced by Pacific waters, extended toward Mendeleev Ridge in 2012–2016 (Bertosio et al., 2022; Regan et al., 2019). Thus, the BG likely contributed to the thickening, freshening, and warming of the UH in the Makarov Basin in 2015.

In 2017, temperatures in the UH were low ($\Theta < -1.4$ °C). Profiles at the beginning of the 2017 trajectory (south Mendeleev Ridge) exhibited a local $\Theta_{max} \sim -1.2$ °C on isopycnal 26.0 kg m⁻³ ($S_A \sim 32.5$ g kg⁻¹), interleaved between two local Θ_{min} at $S_A \sim 31.6$ and 33 g kg⁻¹ (Figures 6l and 7c). This local Θ_{max} was ∼1 g kg⁻¹ saltier and ∼0.8 °C colder compared to the Θ_{max} in 2015, which suggested less influence of Pacific summer waters, as the BG retreated east of the Mendeleev Ridge after 2016 (Bertosio et al., 2022). A similar local Θ_{max} at $S_A \sim 32.5$ g kg⁻¹, observed in 2004 over the nearby Chukchi Abyssal Plain (east of Mendeleev Ridge, Nishino et al., 2008), was attributed to a boundary resulting from the existence of two temperature minima: (a) one on top of the local Θ_{max} and resulting from advected shelf waters formed by winter convection with sea ice formation; (b) one below the local Θ_{max} and attributed to Pacific winter waters influenced by Chukchi Plateau waters and upwelled LH waters. This local Θ_{max} in the UH in 2017 on isopycnal 26 kg m⁻³, along with large vertical salinity gradients, supports a splitting in two sub-layers similar to that documented by Nishino et al. (2008) (at $25 < \sigma < 26$ kg m⁻³ and $26 < \sigma < 26.4$ kg m⁻³, Figures 6c and 6f).
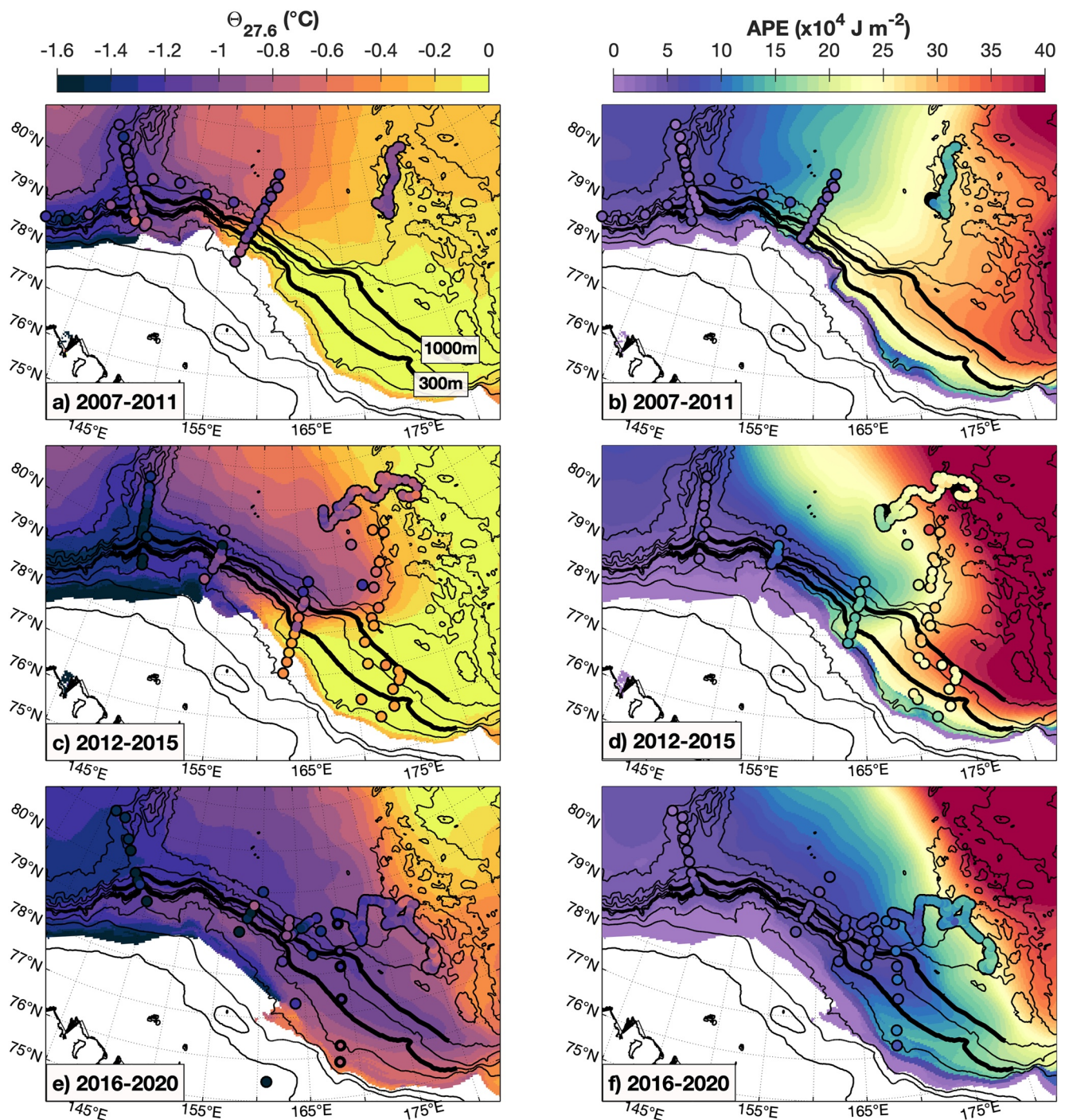
Figure 4. (a, c, e) PSY4 temperature on the 27.6 kg m^{-3} isopycnal, in the lower halocline ($\Theta_{27.6}$, °C). (b, d, f) Available potential energy (APE; 10^4 J m^{-2}). Model values are averaged over (a and b) 2007–2011, (c and d) 2012–2015, and (e and f) 2016–2020. Contemporaneous observed data are in colored circles. Note that PSY4 fields are averaged over several years while observations are synoptic. Isobaths are shown in black lines: thick black lines indicate isobath 300 and 1,000 m.

The base of the UH was cold and associated with low DO values in 2008 and 2015 (DO < 270 μmol kg^{-1}) relative to layers above and below (Figures 7a and 7b), which is a characteristic feature of both Pacific winter waters (Shimada et al., 2005; Timmermans et al., 2010; Woodgate et al., 2005) and ESS waters (Alkire et al., 2019; Anderson et al., 2013). In 2008 and 2015, Alkire et al. (2019) found that the influence of ESS-origin water over the shelf and in Makarov Basin was only visible to the west of 165–170°E, while the influence of western Chukchi Sea waters was found only in the eastern part of the basin. The drifting platforms ITP29 and IAOOS15 were
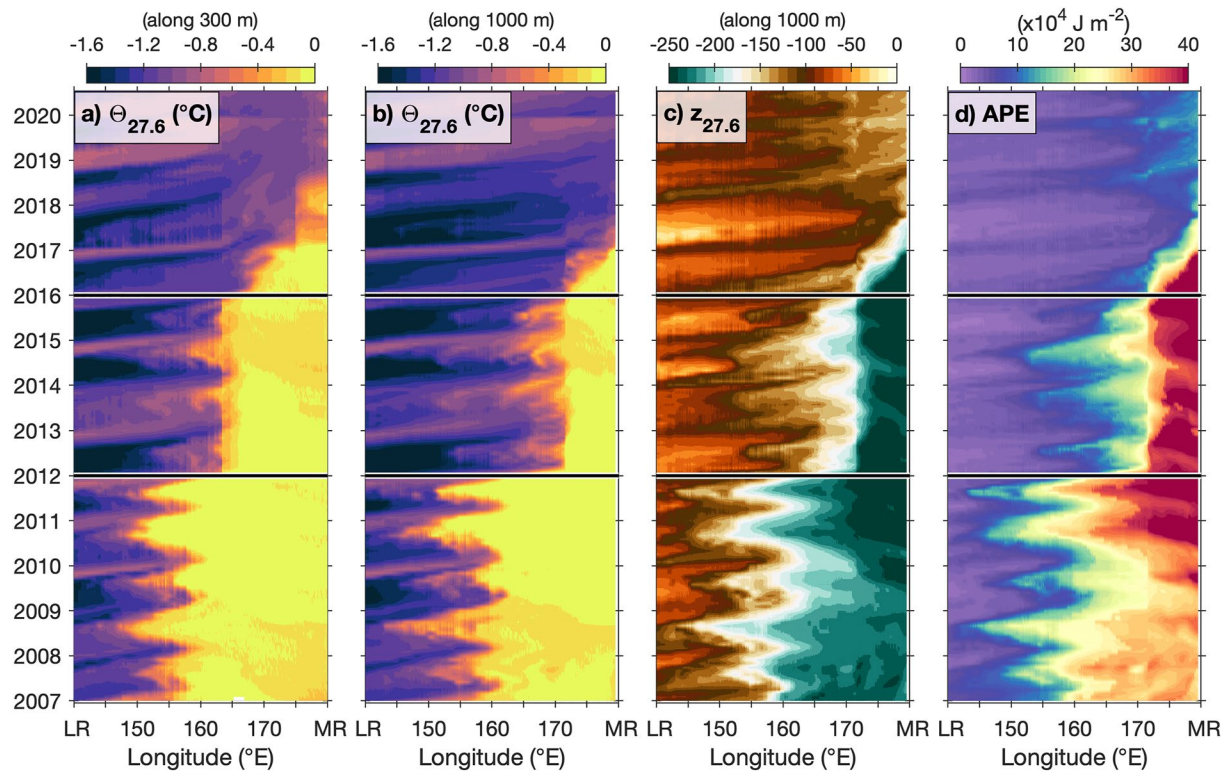
Figure 5. Evolution of 27.6 kg m^{-3} isopycnal temperature $\Theta_{27.6}$ (°C) along isobath (a) 300 m and (b) 1,000 m. (c) Evolution of the depth of the 27.6 kg m^{-3} isopycnal above isobath 1,000 m. (d) Available potential energy (APE; 10^4 J m^{-2}) along isobath 1,000 m. Months of January 2012 and 2016 are indicated by the thick horizontal lines. LR, Lomonosov Ridge; MR, Mendeleev Ridge.

both located east of 165–170°E, suggesting that low-oxygen waters at $S_A \sim 33$ g kg^{-1} were mainly influenced by Pacific winter waters from the western Chukchi Sea.

4.2. Lower Halocline: Evolving Contribution From Atlantic-Origin Waters

In 2008, the LH (27.4 < σ < 27.7 kg m^{-3}) exhibited a sharp bend in the temperature-salinity curve at $S_A \sim 34.4$ g kg^{-1} and $\Theta \sim -1.2$ °C, suggesting a contribution from Atlantic-derived LH resulting from winter convection (Kikuchi et al., 2004; Figure 7a). DO values in the LH, similar to those sampled in the underlying AW layer (DO ~ 290 µmol kg^{-1}, Figure 7a and Table 2) supported an Atlantic origin. The monthly mean of modeled salinity at 150 m in September 2008 displayed values higher than 34.0 g kg^{-1} west of 170°E, where the ITP29 was located, likely corresponding to the salty LH layer (Figure 8a). West of the Lomonosov Ridge, i.e., longitudes less than 140°E, high salinities and relatively low temperatures ($S_A > 34.5$ g kg^{-1}, $\Theta \sim -0.7$ °C) along the continental slope were associated with an eastward current (horizontal velocity $v \sim 7$ cm s^{-1}, Figures 8a and 8b). This salty eastward current broke away from the slope east of the Lomonosov Ridge ($\sim$145°E; 80°N) and entered the Makarov Basin, developing mesoscale structures along the 2,000-m isobath (Figure 8a). This supports the previous assessment that the LH layer of the western part of the Makarov Basin was supplied by salty, Atlantic-derived LH directly from the Eurasian Basin. On the East Siberian shelf, a westward current followed the 300–500-m isobaths and carried water with relatively large temperatures ($\Theta > -0.5$ °C, Figure 8b). East of the Mendeleev Ridge, i.e., east of 180°W, salinity values were lower than 33.2 g kg^{-1} (blue colors in Figure 8a). These relatively fresher waters corresponded to the UH layer, as the UH layer is thicker in the Canada Basin than near the Lomonosov Ridge, reaching as deep as 150 m.

In 2015 and 2017, the Θ-S_A curve obtained from the IAOOS15 and IAOOS25 data exhibited a bend in the LH associated with salinities at $\sim$34.5–34.6 g kg^{-1}, which were higher than that in 2008 ($S_A \sim 34.4$ g kg^{-1}, Figures 7b and 7c). A saltier LH base is a feature also documented in 2017 in the western Eurasian Basin (Bertosio et al., 2020). Temperatures in the LH were between -1.5 and -0.7 °C in 2015 and 2017, which corresponded
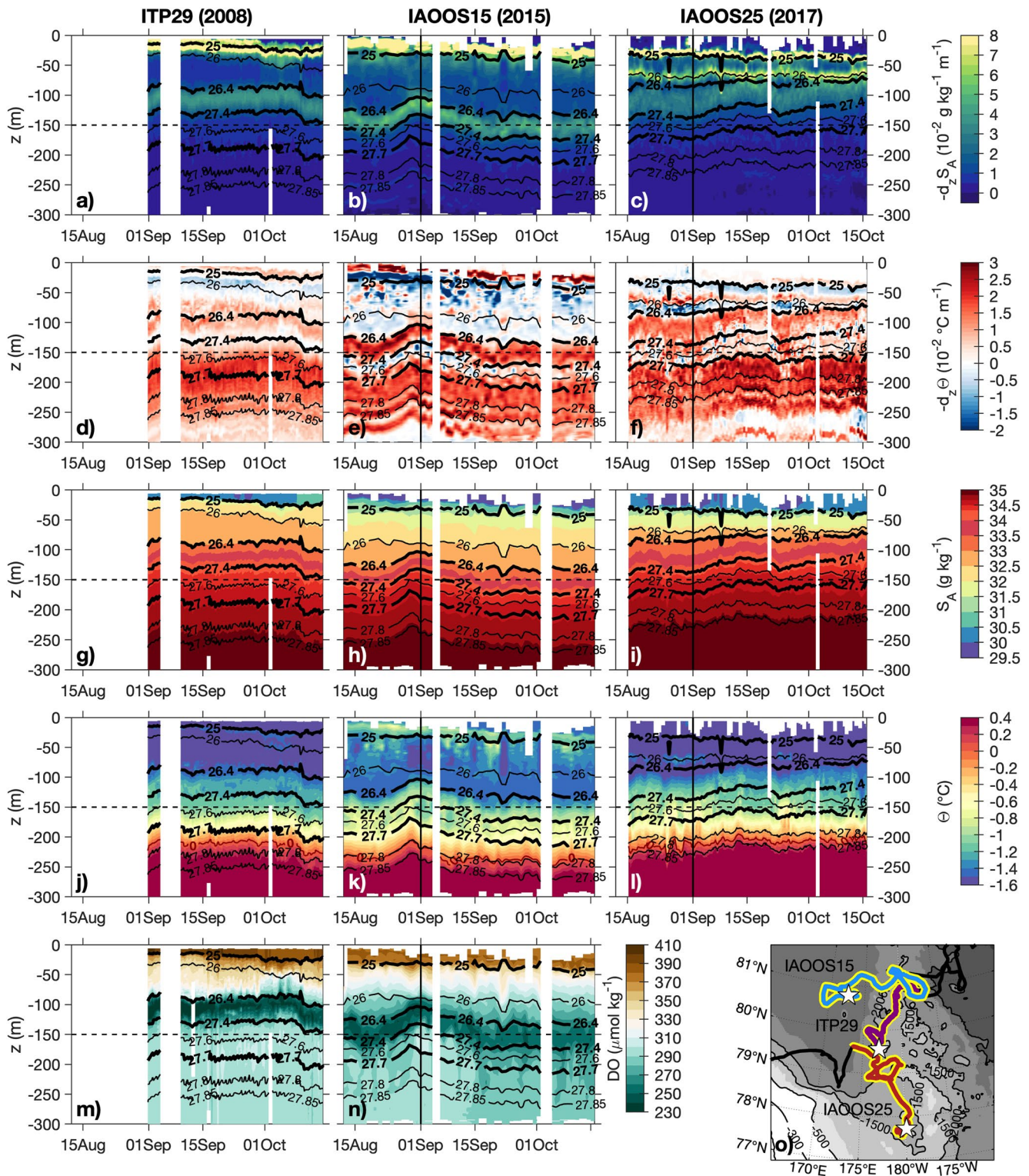
Figure 6. Along-drift profiles from ITP29 (left), IAOOS15 (middle), and IAOOS25 (right): (a, b, c) vertical gradient of absolute salinity (10^{-2} g kg^{-1} m^{-1}), (d, e, f) vertical gradient of conservative temperature (10^{-2} °C m^{-1}), (g, h, i) absolute salinity S_A (g kg^{-1}), (j, k, l) conservative temperature Θ (°C) and (m, n) dissolved oxygen (µmol kg^{-1}). The depth 150 m is indicated by the horizontal dashed line. Isopycnal 25 kg m^{-3} roughly marks the base of the mixed layer, 26.4 kg m^{-3} the base of the upper halocline, and 27.7 kg m^{-3} the base of the lower halocline and upper boundary of Atlantic Waters. (o) Platform trajectories (purple: ITP29; blue: IAOOS15; red: IAOOS25).
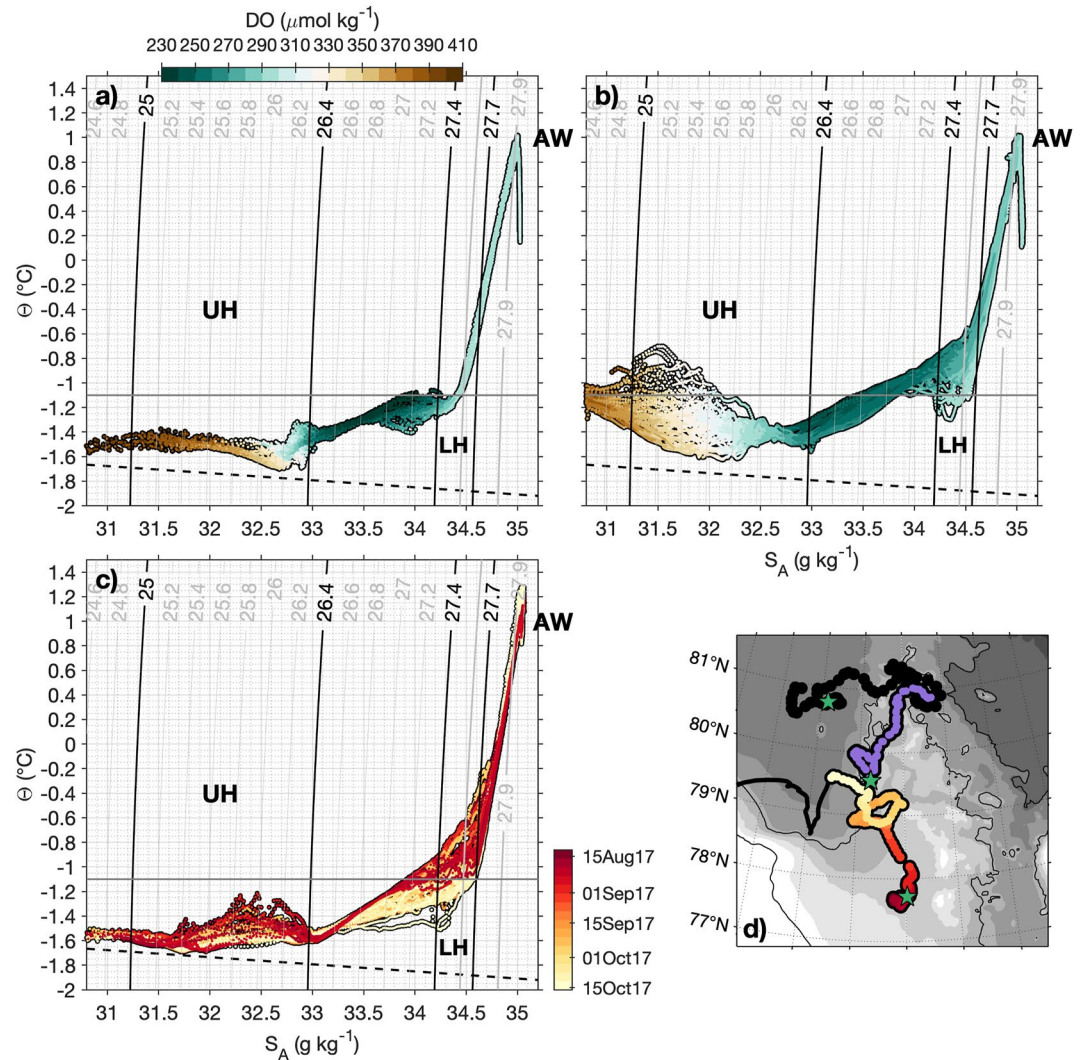
Figure 7. Θ-S_A diagrams from (a) ITP29 (2008), (b) IAOOS15 (2015), and (c) IAOOS25 (2017) data. Dissolved oxygen concentrations in (a) and (b) are in color (μmol kg^{-1}). Time in (c) is in color. The freezing point is the dashed line. (d) Platform trajectories of ITP29 (purple), IAOOS15 (black), and IAOOS25 (color is time as in (c)). Isopycnal 25 kg m^{-3} roughly marks the base of the mixed layer, 26.4 kg m^{-3} the base of the upper halocline (UH), and 27.7 kg m^{-3} the base of the lower halocline (LH) and upper boundary of Atlantic Waters (AW).

to a larger range of values compared to 2008 (Figures 6k, 6l, and 7b, 7c and Table 2). Warm LH waters were associated with a mixing line in the Θ-S_A curve between the base of the UH and AW in 2015 and 2017 (Figure 7b and Table 2), which suggested diapycnal mixing between AW and the overlying Pacific winter water (Wang et al., 2021; Woodgate et al., 2005). In 2015, the warm LH waters exhibited DO values of ~250 μmol kg^{-1}, in contrast with colder LH waters that were associated with higher DO at ~310 μmol kg^{-1} (Figure 7b). This supports the hypothesis that the overlying UH, which is relatively depleted in oxygen, influenced the warm LH. Despite this warming in 2015 and 2017, profiles exhibited cold temperatures in the LH (Θ ~ -1.2 °C), similar to those sampled in 2008, suggesting that some cold Atlantic-derived LH persisted (Figures 7b and 7c).

Model output in September 2015 suggested that the IAOOS15 location corresponded to a strong horizontal salinity front at 150 m (Figure 8). Modeled fields displayed LH saltier than 34.6 g kg^{-1} and colder than -1.2 °C between the continental slope and 81°N (Figures 8c and 8d). A temperature front over the slope was located at ~160–170°E, with colder water to the west compared to the east. The eastward slope current, previously not extending beyond the Lomonosov Ridge, intensified ($v > 7$ cm s^{-1} along the slope) and followed isobath 1,500 m further east until ~175°E. In September 2017, a cold salty LH was found along the continental slope until 180°W

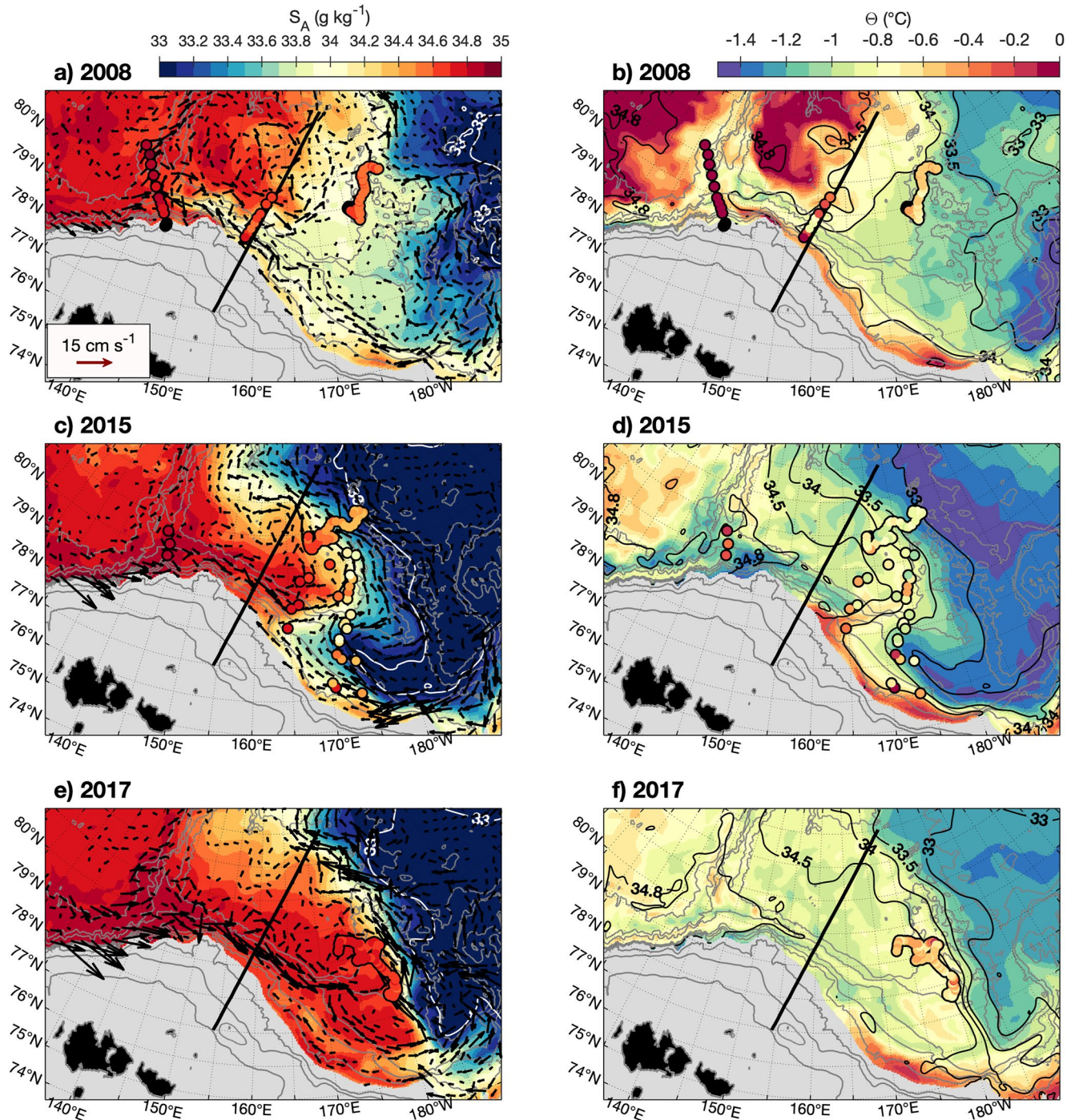**Figure 8.** Monthly mean (left) absolute salinity (S_A, g kg^{-1}) and (right) conservative temperature (Θ, °C) in the lower halocline layer (150 m) in September (a), (b) 2008, (c), (d) 2015, and (e), (f) 2017 in PSY4. In situ values are schematized by colored circles. Monthly mean horizontal velocities (v, cm s^{-1}) larger than 1 cm s^{-1} are shown with arrows. Time evolutions of parameters along the black transect are shown in Figure 9.

and in the entire studied part of the Makarov Basin, including the location of the IAOOS25 (Figures 8e and 8f). The eastward circulation along the continental slope and the northward circulation branch above Mendeleev Ridge were both intensified compared to 2015 ($v > 10$ cm s^{-1}, Figures 8c and 8e).

We focused on a transect across the continental slope (shown in Figure 8) to investigate interannual changes in the slope-basin interaction in the LH (Figure 9). From 2007 until winter 2011–2012, the slope and basin water
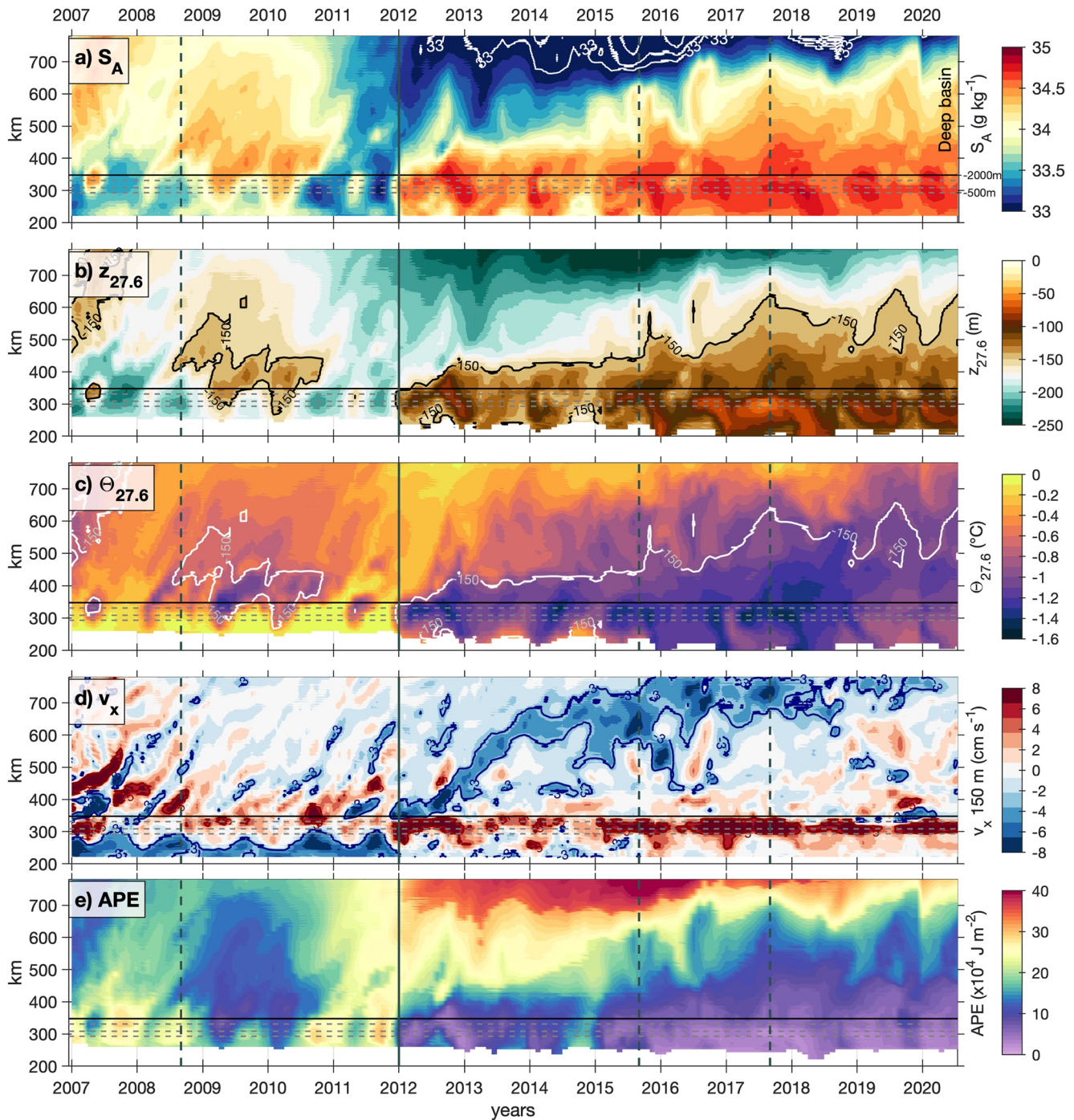
Figure 9. Monthly mean properties along the transect shown in Figure 8. (a) Absolute salinity at 150 m (S_A, g kg^{-1}). (b) Depth of isopycnal 27.6 kg m^{-3} ($z_{27.6}$, m). (c) Conservative temperature on the 27.6 kg m^{-3} isopycnal ($\Theta_{27.6}$, °C). (d) Cross-section velocity at 150 m (v_x, cm s^{-1}) corresponding approximately to the along-slope direction, positive values being oriented south-eastward. (e) Available potential energy (APE, ×10^4 J m^{-2}). September 2008, 2015, and 2017 for which horizontal fields are shown in Figure 8, are marked by vertical dashed lines. January 2012 is marked by a vertical plain line. The position of isobath 2,000 m, which separates the basin from the slope, is indicated by a horizontal thick black line (around km 350). Isobaths 500, 1,000, and 1,500 m are marked by horizontal dashed gray lines (around km 300).

had distinct LH properties: LH was saltier, colder, and deeper in the basin ($S_A > 33.8$ g kg^{-1}, $\Theta_{27.6} < -0.4$ °C, $z_{27.6} \sim 220$ m, Figures 9a–9c), than on the slope. In winter 2011–2012, LH properties strikingly changed on the slope, and the abrupt change coincided with the sharp eastward progression of Atlantic-derived LH: LH became saltier (+1 g kg^{-1}), colder (−1 °C), and shallower (100 m) (Figures 9a–9c). LH properties on-slope
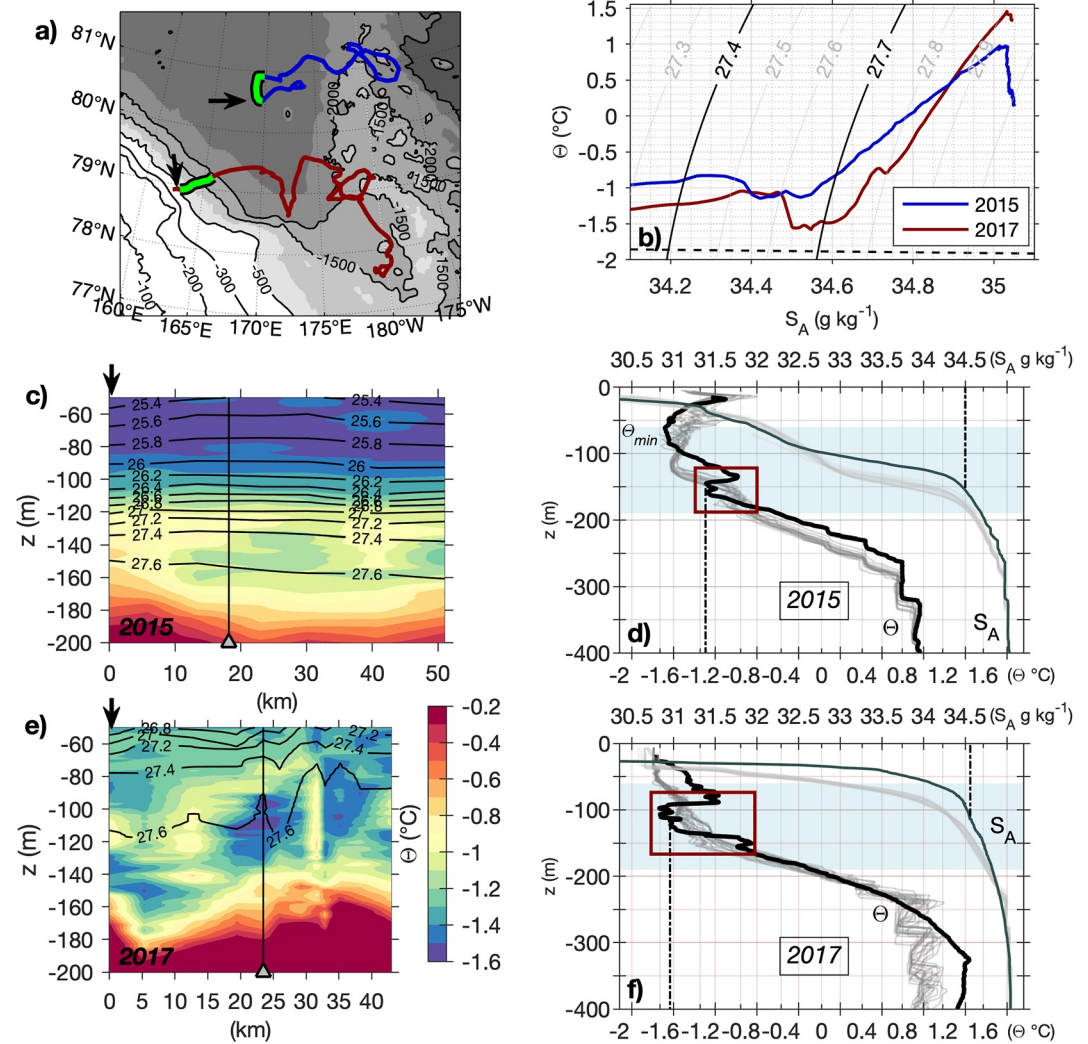
Figure 10. (a) Trajectories of IAOOS15 (blue) and IAOOS25 (red). Cold lenses were found in the green subsections. (b) Temperature-salinity curve in the cold lens for IAOOS15 (blue) and IAOOS25 (dark red). (c) IAOOS15 (September 2015) temperature along the green subsections, and (d) temperature (black thick lines) and salinity (dark gray thick lines) profiles in the cold lens area. The temperature minimum corresponding to the cold core of the lens is highlighted by a red box. (e and f) Same for IAOOS25 (November 2017). The beginning of the section is indicated by an arrow in (a), (c), and (e) and the position of the cold lens is indicated by thick vertical black lines. Light gray profiles in (d) and (f) are outside the cold lens area (15 profiles preceding the green subsection in time) and vertical dotted lines indicate temperature and salinity in the cold lens. The blue shade corresponds to the depths shown in sections (c) and (e). Corresponding synoptic horizontal PSY4 fields are shown in Figure S4 in Supporting Information S1.

were progressively found off-shore from 2012 onwards, indicating active slope-basin exchanges in the LH. A large salinity front located in the deep basin after 2012, associated with westward velocity (along-slope velocity $v_x \sim -7$ cm s^{-1}, Figure 9d), marked the northern limit of slope water influence, and likely corresponded to the boundary of the BG (Bertosio et al., 2022; Regan et al., 2019). From 2012 onwards, large eastward velocities between isobaths 500 and 2,000 m marked the intense slope current ($v_x > 8$ cm s^{-1}, Figure 9d). In parallel, the water column stratification weakened along the slope from 2012 onwards, and progressively northward in the Makarov Basin (APE < 10 ×10^4 J m^{-2}, Figure 9e). Note that APE > 30 ×10^4 J m^{-2} found off-shore from 2012 to 2018 is consistent with the influence of the BG, inside which APE can be higher than 20 × 10^4 J m^{-2} (Polyakov et al., 2018).

Table 2
Hydrographic Characteristics in the Makarov Basin During Summers 2008, 2015, and 2017

Layer	σ (kg m^{-3})		ITP29 (2008)		IAOOS15 (2015)		IAOOS25 (2017)	
Upper halocline	[25; 26.4]	z	55	[20; 90]	80	[20; 130]	60	[20; 80]
		S_A	32.5	[31; 33]	32.3	[31; 33]	32.1	[31; 33]
		Θ	−1.6	[−1.7; 1.3]	−1.4	[−1.6; −0.7]	−1.6	[−1.7; −1.2]
		DO	330	[238; 410]	304	[242; 381]		
Intermediate layer	[26.4; 27.4]	z	110	[90; 140]	145	[130; 180]	100	[80; 130]
		S_A	33.6	[33; 34.2]	33.6	[33; 34.2]	33.6	[33; 34.2]
		Θ	−1.3	[−1.6; −1.1]	−1.4	[−1.6; −0.8]	−1.3	[−1.6; −0.9]
		DO	250	[219; 296]	250	[239; 297]		
Lower halocline	[27.4; 27.7]	z	160	[140; 190]	190	[180; 200]	145	[130; 160]
		S_A	34.5	[34.2; 34.6]	34.5	[34.2; 34.6]	34.5	[34.2; 34.6]
		Θ	−1.2	[−1.3; −1.1]	−0.9	[−1.3; −0.7]	−1.1	[−1.5; −0.7]
		DO	290	[250; 300]	270	[240; 300]		
Thermocline	[27.7; 27.85]	z	210	[190; 260]	220	[200; 260]	180	[160; 220]
		S_A	34.8	[34.6; 34.9]	34.8	[34.6; 34.9]	34.8	[34.6; 34.9]
		Θ	−0.1	[−1; 0.7]	−0.3	[−1.1; 0.8]	−0.5	[−1.2; 0.6]
		DO	297	[283; 311]	286	[261; 303]		
Top Atlantic layer	~27.85	z	260		260		220	
		S_A	34.9		34.9		34.9	
		Θ	0.6		0.4		0.2	
		DO	295		287			

Note. Boundaries in density (σ, kg m^{-3}) are given for each layer, together with the mean observed properties: Depth (z, m), absolute salinity (S_A, g kg^{-1}), conservative temperature (Θ, °C), and dissolved oxygen (DO, μmol kg^{-1}). Minimum and maximum values are given in square brackets.

4.3. Cold-Core Mesoscale Lenses Within the Lower Halocline

Two cold-water lenses were observed in the LH in 2015 and 2017 (respectively in IAOOS15 and IAOOS25 data, Figure 10). The first one was sampled from 31 August to 3 September 2015, around 169°E, 80.6°N, between isopycnals 27.4 and 27.7 kg m^{-3} in the Makarov Basin (green part of the IAOOS15 trajectory in Figures 10a, 10c, and 10d). The second one was found near the continental slope (164°E, 79°N), between isopycnals 27.6 and 27.8 kg m^{-3}, above the 1,500-m isobath, and sampled from 13 to 16 November 2017 (Figures 6, 10e, and 10f). In 2015 (respectively, 2017), the lens, located at 120–170-m depth (100–140 m), had a horizontal scale of 40 km (20 km) and a core temperature of −1.3 °C (−1.5 °C) colder than the surrounding waters ($\Theta \sim -0.8$ °C, Figures 10c–10f). Both cold mesoscale lenses were associated with a shoaling of isopycnals (Figures 6b and 6d).

In 2015, the cold lens was located below a cold UH centered on a $\Theta_{min} \sim -1.6$ °C at 60 m (thick black profile, Figure 10d). In contrast, there were no cold lenses in the LH in the other profiles sampled by the platform that year in the basin and the UH exhibited a deeper $\Theta_{min} \sim -1.5$ °C at 140 m (thin gray profiles, Figure 10d). This indicated that the water column associated with the cold lens in 2015 was different from the rest of the basin, possibly resulting from different source contributions at this precise location. In 2017, the UH overlying the cold-water lens at the East Siberian slope, above 100 m, was warmer than the surrounding water and did not exhibit a Θ_{min} (Figure 10f).

Modeled horizontal velocity fields averaged in September 2015 displayed a large salty cyclonic branch detaching from the intensified slope current and crossing the IAOOS15 trajectory in the Makarov Basin, where the cold mesoscale lens was sampled in the LH (Figures 8c and 10 and see Figure S4a in Supporting Information S1 for the synoptic map). In November 2017, PSY4 suggested that the cold lens sampled by the IAOOS25 was encountered on the continental slope after the Atlantic-derived LH had shifted eastward along the slope (Figure 8e and Figure S4b in Supporting Information S1). This suggested that the two cold mesoscale lenses were composed of
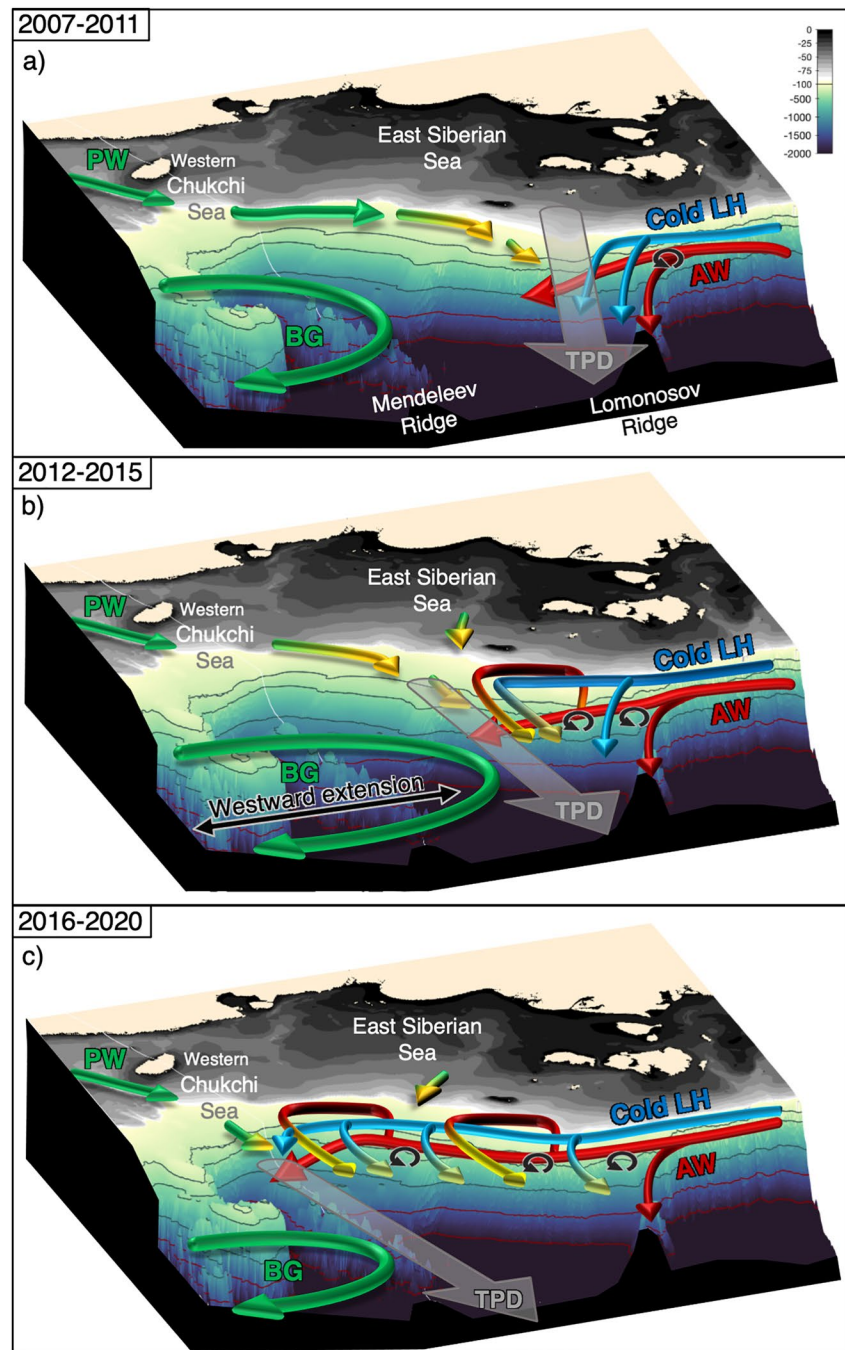
Figure 11. Schematics of halocline water circulation along the East Siberian Sea slope (ESS) and in the Makarov Basin during the periods (a) 2007–2011, (b) 2012–2015, and (c) 2016–2020. The eastward progression of the relatively cold Atlantic-derived lower halocline (LH) waters, influencing the Makarov Basin lower halocline, is shown in blue arrows. The underlying Atlantic Water (AW, red arrows) upwells over the slope and mixes with shelf waters (in yellow), forming warmer LH waters. The mesoscale activity, increasing to the east and contributing to enhancing slope water influence in the Makarov Basin interior, is represented in black arrows. The Beaufort Gyre (BG) extended westward in 2012–2015 and likely brought additional contributions of Pacific Water (PW, green arrows) to the upper halocline in the Makarov Basin. In 2016–2020, the BG retreated to the east, and the Transpolar Drift (TPD, gray arrow) shifted toward Mendeleev Ridge.

cold Atlantic-derived LH water from the Eurasian Basin that flowed along the slope of the East Siberian shelf. From 2007 onwards, the strengthening of the boundary current along the continental slope likely contributed to the shedding of mesoscale lenses and eddies in the Makarov Basin. Similar processes have been observed near

the Atlantic Water Boundary Current in the Eurasian Basin (e.g., Athanase et al., 2019, 2021; Pérez-Hernández et al., 2017). Our study suggests these cold mesoscale lenses detaching from the slope current likely increased the contribution of Atlantic-derived waters from the slope to the LH in the Makarov Basin (Figures 8a, 8c, 8e, and 9d).

5. Summary and Conclusion

We examined the evolution of the halocline in the Makarov Basin and along the East Siberian Sea (ESS) slope, combining in situ measurements and modeled fields from the operational physical model PSY4. Mercator Ocean simulations were highly complementary to the hydrographic measurements and provided valuable insights into the evolution of the halocline in the Makarov Basin and along the East Siberian continental slope. Figure 11 summarizes our findings. We identified three distinct periods.

During the 2007–2011 period (Figure 11a), the upper halocline (UH) in the western Makarov Basin was influenced by ESS waters (e.g., Alkire et al., 2019; Anderson et al., 2013) and by western Chukchi Sea Pacific waters near Mendeleev Ridge. The underlying lower halocline (LH) was cold and mainly comprised Atlantic-derived LH entering the Makarov Basin near the Lomonosov Ridge. At that time, relatively shallow and cold Atlantic-derived LH was documented west of ~155–160°E, along the East Siberian continental slope.

During 2012–2015 (Figure 11b), Makarov Basin UH properties (thicker layer, warmer and fresher) were consistent with the presence of Pacific water from the Chukchi Plateau, driven by the westward extension of the BG (e.g., Alkire et al., 2019; Nishino et al., 2013; Proshutinsky et al., 2019; Regan et al., 2019). In winter 2012, cold Atlantic-derived LH abruptly shifted eastward along the East Siberian continental shelf and slope (from 155°E to 170°E, above the 1,000-m isobath), causing a reduction in the halocline strength along the slope. Upwelled AW along the slope mixed with bottom shelf waters and formed warmer LH. From 2012 onwards, the velocity along the continental slope increased, and the enhanced boundary current was observed to shed mesoscale structures in the LH, toward the Makarov Basin. Drifting platform data and PSY4 fields suggested that these mesoscale structures observed east of 164°E in 2015 and 2017 comprised cold Atlantic-derived lower halocline waters. The shedding of mesoscale lenses from the slope current likely increased the contribution of Atlantic-derived lower halocline water to the LH of the Makarov Basin. Atlantic Water, thus, influenced the Makarov Basin LH in two ways: (a) with cold Atlantic-derived LH from the Eurasian Basin and (b) with warm LH resulting from diapycnal mixing on the slope with shelf waters. Concomitantly, the halocline weakened in the basin.

After 2016 (Figure 11c), the BG was located further east (Bertosio et al., 2022) and Makarov Basin UH properties differed from previous years: the cold UH likely resulted from advected fresh East Siberian cold shelf water (Alkire et al., 2019; Wang et al., 2021) or fresh Pacific winter waters (Woodgate & Peralta-Ferriz, 2021). In parallel, cold Atlantic-derived LH reached the western Chukchi Sea, which is consistent with the high-salinity cold waters found south of Mendeleev Ridge in summer 2017 at 120–150 m by Jung et al. (2021). In the meantime, the halocline strength along the slope of the East Siberian shelf was similar to that of the Eurasian Basin.

Our study suggests that the weakening of the halocline along the East Siberian continental slope and in the Makarov Basin is related to an increased contribution of Atlantic-derived waters into the LH. Polyakov et al. (2017, 2020) showed that the weakening of the halocline resulted from the gradual shoaling of the AW in the Eurasian Basin (a process called "Atlantification"). Here, we show that a similar process is now impacting the western Amerasian Basin, reaching the Chukchi Borderland.

Data Availability Statement

ITP data are available on the *Beaufort Gyre Exploration Project* website (https://www2.whoi.edu/site/beaufort-gyre/data/; Krishfield et al., 2008; Proshutinsky et al., 2009). IAOOS data are available on *SEANOE* (Bertosio et al., 2021). NABOS and SWERUS data are available on the Arctic Data Center website (NABOS, 2007, 2008: https://arcticdata.io/catalog/view/dfbf7fa6-6aed-403b-b188-3e308270a779; NABOS-II: https://arctic-data.io/catalog/view/doi%3A10.18739/A20C4SK4J; NABOS, 2018: https://arcticdata.io/catalog/view/doi%3A10.18739/A2X34MS0V; SWERUS https://arcticdata.io/catalog/view/doi:10.18739/A2CZ9N). Data from the Korean campaign are available on the KOPRI data servers (https://kpdc.kopri.re.kr/search/80785502-2cb4-4146-a799-b7c76d65f47c). The data from the Russian campaign in 2016 can be obtained at the following

website: https://zenodo.org/record/4507584#.Yv0GHvHP0ds. The model outputs are available at Copernicus Marine Environment Monitoring Service (CMEMS; http://marine.copernicus.eu/).

References

Alkire, M. B., Rember, R., & Polyakov, I. (2019). Discrepancy in the identification of the Atlantic/Pacific Front in the Central Arctic Ocean: NO versus nutrient relationships. *Geophysical Research Letters*, *46*, 3843–3852. https://doi.org/10.1029/2018GL081837

Anderson, L. G., Andersson, P. S., Björk, G., Jones, E. P., Jutterström, S., & Wåhlström, I. (2013). Source and formation of the upper halocline of the Arctic Ocean. *Journal of Geophysical Research: Oceans*, *118*, 410–421. https://doi.org/10.1029/2012JC008291

Anderson, L. G., Björk, G., Holby, O., Jutterström, S., Mörth, C. M., O'Regan, M., et al. (2017). Shelf-basin interaction along the East Siberian Sea. *Ocean Science*, *13*(2), 349–363. https://doi.org/10.5194/os-13-349-2017

Anderson, L. G., Björk, G., Jutterström, S., Pipko, I., Shakhova, N., Semiletov, I., & Wåhlström, I. (2011). East Siberian Sea, an Arctic region of very high biogeochemical activity. *Biogeosciences*, *8*(6), 1745–1754. https://doi.org/10.5194/bg-8-1745-2011

Athanase, M., Provost, C., Artana, C., Pérez-Hernández, M. D., Sennéchael, N., Bertosio, C., et al. (2021). Changes in Atlantic Water circulation patterns and volume transports North of Svalbard over the last 12 years (2008–2020). *Journal of Geophysical Research: Oceans*, *126*, e2020JC016825. https://doi.org/10.1029/2020JC016825

Athanase, M., Provost, C., Pérez-Hernández, M. D., Sennéchael, N., Bertosio, C., Artana, C., et al. (2020). Atlantic water modification north of Svalbard in the Mercator physical system from 2007 to 2020. *Journal of Geophysical Research: Oceans*, *125*, e2020JC016463. https://doi.org/10.1029/2020JC016463

Athanase, M., Sennéchael, N., Garric, G., Koenig, Z., Boles, E., & Provost, C. (2019). New hydrographic measurements of the upper arctic western Eurasian Basin in 2017 reveal fresher mixed layer and shallower warm layer than 2005–2012 climatology. *Journal of Geophysical Research: Oceans*, *124*, 1091–1114. https://doi.org/10.1029/2018JC014701

Bauch, D., & Cherniavskaia, E. (2018). Water mass classification on a highly variable arctic shelf region: Origin of Laptev Sea water masses and implications for the nutrient budget. *Journal of Geophysical Research: Oceans*, *123*, 1896–1906. https://doi.org/10.1002/2017JC013524

Bauch, D., Cherniavskaia, E., & Timokhov, L. (2016). Shelf basin exchange along the Siberian continental margin: Modification of Atlantic water and lower halocline water. *Deep Sea Research Part I: Oceanographic Research Papers*, *115*, 188–198. https://doi.org/10.1016/j.dsr.2016.06.008

Bertosio, C., Provost, C., Athanase, M., Sennéchael, N., Lellouche, J.-M., Garric, G., et al. (2022). Changes in freshwater distribution and pathways in the Arctic Ocean since 2007 in the Mercator Ocean global operational system. *Journal of Geophysical Research: Oceans*, *127*, e2021JC017701. https://doi.org/10.1029/2021JC017701

Bertosio, C., Provost, C., Sennéchael, N., Artana, C., Athanase, M., Boles, E., et al. (2020). The western Eurasian Basin halocline in 2017: Insights from autonomous NO measurements and the Mercator physical system. *Journal of Geophysical Research: Oceans*, *125*, e2020JC016204. https://doi.org/10.1029/2020JC016204

Bertosio, C., Provost, C., Sennéchael, N., Koenig, Z., Labaste, M., & Athanase, M. (2021). *Arctic Makarov Basin: IAOOS14, IAOOS15 and IAOOS25 ocean CTD-DO profiles in 2015 and 2017*. SEANOE. https://doi.org/10.17882/83520

Bourgain, P., & Gascard, J. C. (2011). The Arctic Ocean halocline and its interannual variability from 1997 to 2008. *Deep Sea Research Part I: Oceanographic Research Papers*, *58*(7), 745–756. https://doi.org/10.1016/j.dsr.2011.05.001

Bourgain, P., & Gascard, J. C. (2012). The Atlantic and summer Pacific waters variability in the Arctic Ocean from 1997 to 2008. *Geophysical Research Letters*, *39*, L05603. https://doi.org/10.1029/2012GL051045

Carmack, E. C. (2007). The alpha/beta ocean distinction: A perspective on freshwater fluxes, convection, nutrients and productivity in high-latitude seas. *Deep-Sea Research II*, *54*, 2578–2598. https://doi.org/10.1016/j.dsr2.2007.08.018

Carmack, E. C., Yamamoto-Kawai, M., Haine, T. W. N., Bacon, S., Bluhm, B. A., Lique, C., et al. (2016). Freshwater and its role in the Arctic Marine System: Sources, disposition, storage, export, and physical and biogeochemical consequences in the Arctic and global oceans. *Journal of Geophysical Research: Biogeosciences*, *121*, 675–717. https://doi.org/10.1002/2015JG003140

Colin Verdière, de, A., Huck, T., Pogossian, S., & Ollitrault, M. (2018). Available potential energy in density coordinates. *Journal of Physical Oceanography*, *48*(8), 1867–1883. https://doi.org/10.1175/JPO-D-17-0272.1

Dmitrenko, I. A., Ivanov, V. V., Kirillov, S. A., Vinogradova, E. L., Torres-Valdes, S., & Bauch, D. (2011). Properties of the Atlantic derived halocline waters over the Laptev Sea continental margin: Evidence from 2002 to 2009. *Journal of Geophysical Research*, *116*, C10024. https://doi.org/10.1029/2011JC007269

Feistel, R. (2018). Thermodynamic properties of seawater, ice and humid air: TEOS-10, before and beyond. *Ocean Science*, *14*(3), 471–502. https://doi.org/10.5194/os-14-471-2018

Fer, I., Koenig, Z., Kozlov, I. E., Ostrowski, M., Rippeth, T. P., Padman, L., et al. (2020). Tidally forced lee waves drive turbulent mixing along the Arctic Ocean margins. *Geophysical Research Letters*, *47*, e2020GL088083. https://doi.org/10.1029/2020GL088083

Fichefet, T., & Maqueda, M. A. (1997). Sensitivity of a global sea ice model to the treatment of ice thermodynamics and dynamics. *Journal of Geophysical Research*, *102*, 12609–12646. https://doi.org/10.1029/97JC00480

Haine, T. W. N., Curry, B., Gerdes, R., Hansen, E., Karcher, M., Lee, C., et al. (2015). Arctic freshwater export: Status, mechanisms, and prospects. *Global and Planetary Change*, *125*, 13–35. https://doi.org/10.1016/j.gloplacha.2014.11.013

Jung, J., Cho, K.-H., Park, T., Yoshizawa, E., Lee, Y., Yang, E. J., et al. (2021). Atlantic-origin cold saline water intrusion and shoaling of the nutricline in the Pacific Arctic. *Geophysical Research Letters*, *48*, e2020GL090907. https://doi.org/10.1029/2020GL090907

Kikuchi, T., Hatakeyama, K., & Morison, J. H. (2004). Distribution of convective lower halocline water in the eastern Arctic Ocean. *Journal of Geophysical Research*, *109*, C12030. https://doi.org/10.1029/2003JC002223

Koenig, Z., Provost, C., Sennéchael, N., Garric, G., & Gascard, J.-C. (2017). The Yermak Pass branch: A major pathway for the Atlantic water north of Svalbard? *Journal of Geophysical Research: Oceans*, *122*, 9332–9349. https://doi.org/10.1002/2017JC013271

Koenig, Z., Provost, C., Villacieros-Robineau, N., Sennéchael, N., Meyer, A., Lellouche, J.-M., & Garric, G. (2017). Atlantic waters inflow north of Svalbard: Insights from IAOOS observations and Mercator Ocean global operational system during N-ICE2015. *Journal of Geophysical Research: Oceans*, *122*, 1254–1273. https://doi.org/10.1002/2016JC012424

Krishfield, R., Toole, J., Proshutinsky, A., & Timmermans, M.-L. (2008). Automated ice-tethered profilers for seawater observations under pack ice in all seasons. *Journal of Atmospheric and Oceanic Technology*, *25*(11), 2091–2105. https://doi.org/10.1175/2008JTECHO587.1

Lellouche, J.-M., Greiner, E., Galloudec, O. L., Garric, G., Regnier, C., Drevillon, M., et al. (2018). Recent updates to the Copernicus Marine Service global ocean monitoring and forecasting real-time 1/12° high-resolution system. *Ocean Science*, *14*(5), 1093–1126. https://doi.org/10.5194/os-14-1093-2018

Lenn, Y. D., Wiles, P. J., Torres-Valdes, S., Abrahamsen, E. P., Rippeth, T. P., Simpson, J. H., et al. (2009). Vertical mixing at intermediate depths in the Arctic boundary current. *Geophysical Research Letters*, *36*, L05601. https://doi.org/10.1029/2008GL036792

Madec, G., & Imbard, M. (1996). A global ocean mesh to overcome the North Pole singularity. *Climate Dynamics*, *12*, 381–388. https://doi.org/10.1007/bf00211684

Madec, G., & the NEMO Team: NEMO Ocean Engine. (2008). *Note du Pôle de modélisation* (Vol. 27, pp. 1288–1619). France: Institut Pierre-Simon Laplace (IPSL).

McDougall, T. J., & Barker, P. M. (2011). *Getting started with TEOS-10 and the Gibbs Seawater (GSW) Oceanographic Toolbox* (p. 28). SCOR/IAPSO WG127.

McLaughlin, F. A., Carmack, E. C., Macdonald, R. W., Melling, H., Swift, J. H., Wheeler, P. A., et al. (2004). The joint roles of Pacific and Atlantic-origin waters in the Canada Basin, 1997–1998. *Deep Sea Research Part I: Oceanographic Research Papers*, *51*(1), 107–128. https://doi.org/10.1016/j.dsr.2003.09.010

Morison, J., Kwok, R., Peralta-Ferriz, C., Alkire, M., Rigor, I., Andersen, R., & Steele, M. (2012). Changing Arctic Ocean freshwater pathways. *Nature*, *481*(7379), 66–70. https://doi.org/10.1038/nature10705

Morison, J., Steele, M., & Andersen, R. (1998). Hydrography of the upper Arctic Ocean measured from the nuclear submarine U.S.S. Pargo. *Deep Sea Research Part I: Oceanographic Research Papers*, *45*(1), 15–38. https://doi.org/10.1016/S0967-0637(97)00025-3

NABOS. (2007). Retrieved from https://arcticdata.io/catalog/view/dfbf7fa6-6aed-403b-b188-3e308270a779

NABOS. (2008). Retrieved from https://arcticdata.io/catalog/view/dfbf7fa6-6aed-403b-b188-3e308270a779

NABOS. (2015). NABOS-II. Retrieved from https://arcticdata.io/catalog/view/doi%3A10.18739/A20C4SK4J

NABOS. (2018). Retrieved from https://arcticdata.io/catalog/view/doi%3A10.18739/A2X34MS0V

Nishino, S., Itoh, M., Williams, W. J., & Semiletov, I. (2013). Shoaling of the nutricline with an increase in near-freezing temperature water in the Makarov Basin. *Journal of Geophysical Research: Oceans*, *118*, 635–649. https://doi.org/10.1029/2012JC008234

Nishino, S., Shimada, K., Itoh, M., Yamamoto-Kawai, M., & Chiba, S. (2008). East–west differences in water mass, nutrient, and chlorophyll a distributions in the sea ice reduction region of the western Arctic Ocean. *Journal of Geophysical Research*, *113*, C00A01. https://doi.org/10.1029/2007JC004666

Peralta-Ferriz, C., & Woodgate, R. A. (2017). The dominant role of the east Siberian Sea in driving the oceanic flow through the Bering Strait—Conclusions from GRACE ocean mass satellite data and in situ mooring observations between 2002 and 2016. *Geophysical Research Letters*, *44*, 11472–11481. https://doi.org/10.1002/2017GL075179

Pérez-Hernández, M. D., Pickart, R. S., Pavlov, V., Våge, K., Ingvaldsen, R., Sundfjord, A., & Falk-Petersen, S. (2017). The Atlantic Water boundary current north of Svalbard in late summer. *Journal of Geophysical Research: Oceans*, *122*, 2269–1716. https://doi.org/10.1029/2018JC014299

Pisareva, M. N., Pickart, R. S., Spall, M. A., Nobre, C., Torres, D. J., Moore, G. W. K., & Whitledge, T. E. (2015). Flow of pacific water in the western Chukchi Sea: Results from the 2009 RUSALCA expedition. *Deep Sea Research Part I: Oceanographic Research Papers*, *105*, 53–73. https://doi.org/10.1016/j.dsr.2015.08.011

Polyakov, I. V., Pnyushkov, A. V., Alkire, M. B., Ashik, I. M., Baumann, T. M., Carmack, E. C., et al. (2017). Greater role for Atlantic inflows on sea ice loss in the Eurasian Basin of the Arctic Ocean. *Science*, *356*(6335), 285–291. https://doi.org/10.1126/science.aai8204

Polyakov, I. V., Pnyushkov, A. V., & Carmack, E. C. (2018). Stability of the Arctic halocline: A new indicator of arctic climate change. *Environmental Research Letters*, *13*(12), 125008. https://doi.org/10.1088/1748-9326/aaec1e

Polyakov, I. V., Rippeth, T. P., Fer, I., Alkire, M. B., Baumann, T. M., Carmack, E. C., et al. (2020). Weakening of cold halocline layer exposes sea Ice to oceanic heat in the eastern Arctic Ocean. *Journal of Climate*, *33*(18), 8107–8123. https://doi.org/10.1175/JCLI-D-19-0976.1

Proshutinsky, A., Krishfield, R., Timmermans, M.-L., Toole, J., Carmack, E. C., McLaughlin, F., et al. (2009). Beaufort Gyre freshwater reservoir: State and variability from observations. *Journal of Geophysical Research*, *114*, C00A10. https://doi.org/10.1029/2008JC005104

Proshutinsky, A., Krishfield, R., Toole, J. M., Timmermans, M.-L., Williams, W., Zimmermann, S., et al. (2019). Analysis of the Beaufort Gyre freshwater content in 2003–2018. *Journal of Geophysical Research: Oceans*, *124*, 9658–9689. https://doi.org/10.1029/2019JC015281

Rainville, L., & Winsor, P. (2008). Mixing across the Arctic Ocean: Microstructure observations during the Beringia 2005 Expedition. *Geophysical Research Letters*, *35*, L08606. https://doi.org/10.1029/2008GL033532

Regan, H., Lique, C., & Armitage, T. W. K. (2019). The Beaufort Gyre extent, shape, and location between 2003 and 2014 from satellite observations. *Journal of Geophysical Research: Oceans*, *124*, 844–862. https://doi.org/10.1029/2018JC014379

Rudels, B., Anderson, L. G., & Jones, E. P. (1996). Formation and evolution of the surface mixed layer and halocline of the Arctic Ocean. *Journal of Geophysical Research*, *101*(C4), 8807–8821. https://doi.org/10.1029/96JC00143

Rudels, B., Korhonen, M., Schauer, U., Pisarev, S., Rabe, B., & Wisotzki, A. (2015). Circulation and transformation of Atlantic water in the Eurasian Basin and the contribution of the Fram Strait inflow branch to the Arctic Ocean heat budget. *Progress in Oceanography*, *132*, 128–152. https://doi.org/10.1016/j.pocean.2014.04.003

Rudels, B., Meyer, R., Fahrbach, E., Ivanov, V. V., Østerhus, S., Quadfasel, D., et al. (2000). Water mass distribution in Fram Strait and over the Yermak Plateau in summer 1997. *Annales Geophysical*, *18*(6), 687–705. https://doi.org/10.1007/s00585-000-0687-5

Schulz, K., Büttner, S., Rogge, A., Janout, M., Hölemann, J., & Rippeth, T. P. (2021a). Turbulent mixing and the formation of an intermediate nepheloid layer above the Siberian continental shelf break. *Geophysical Research Letters*, *48*, e2021GL092988. https://doi.org/10.1029/2021GL092988

Schulz, K., Janout, M., Lenn, Y.-D., Ruiz-Castillo, E., Polyakov, I., Mohrholz, V., et al. (2021b). On the along-slope heat loss of the Boundary Current in the Eastern Arctic Ocean. *Journal of Geophysical Research: Oceans*, *126*, e2020JC016375. https://doi.org/10.1029/2020JC016375

Serreze, M. C., Barrett, A. P., Crawford, A. D., & Woodgate, R. A. (2019). Monthly variability in Bering Strait oceanic volume and heat transports, links to atmospheric circulation and ocean temperature, and implications for sea ice conditions. *Journal of Geophysical Research: Oceans*, *124*(12), 9317–9337. https://doi.org/10.1029/2019JC015422

Shimada, K., Carmack, E. C., Hatakeyama, K., & Takizawa, T. (2001). Varieties of shallow temperature maximum waters in the western Canadian Basin of the Arctic Ocean. *Geophysical Research Letters*, *28*(18), 3441–3444. https://doi.org/10.1029/2001GL013168

Shimada, K., Itoh, M., Nishino, S., McLaughlin, F., Carmack, E. C., & Proshutinsky, A. (2005). Halocline structure in the Canada Basin of the Arctic Ocean. *Geophysical Research Letters*, *32*, L03605. https://doi.org/10.1029/2004GL021358

Steele, M., & Boyd, T. (1998). Retreat of the cold halocline layer in the Arctic Ocean. *Journal of Geophysical Research*, *103*(C5), 10419–10435. https://doi.org/10.1029/98JC00580

Steele, M., Morison, J., Ermold, W., Rigor, I., Ortmeyer, M., & Shimada, K. (2004). Circulation of summer Pacific halocline water in the Arctic Ocean. *Journal of Geophysical Research*, *109*, C02027. https://doi.org/10.1029/2003JC002009

Swift, J. H., Jones, E. P., Aagaard, K., Carmack, E. C., Hingston, M., MacDonald, R. W., et al. (1997). Waters of the Makarov and Canada basins. *Deep Sea Research Part II: Topical Studies in Oceanography*, *44*(8), 1503–1529. https://doi.org/10.1016/S0967-0645(97)00055-6

Timmermans, M.-L., Cole, S., & Toole, J. (2012). Horizontal density structure and restratification of the Arctic Ocean surface layer. *Journal of Physical Oceanography*, *42*(4), 659–668. https://doi.org/10.1175/JPO-D-11-0125.1

Timmermans, M. L., & Jayne, S. R. (2016). The Arctic Ocean spices up. *Journal of Physical Oceanography*, *46*(4), 1277–1284. https://doi.org/10.1175/jpo-d-16-0027.1

Timmermans, M.-L., Krishfield, R., Laney, S., & Toole, J. (2010). Ice-tethered profiler measurements of dissolved oxygen under permanent ice cover in the Arctic Ocean. *Journal of Atmospheric and Oceanic Technology*, *27*(11), 1936–1949. https://doi.org/10.1175/2010JTECHO772.1

Timmermans, M.-L., Marshall, J., Proshutinsky, A., & Scott, J. (2017). Seasonally derived components of the Canada Basin halocline. *Geophysical Research Letters*, *44*, 5008–5015. https://doi.org/10.1002/2017GL073042

Timmermans, M.-L., Proshutinsky, A., Golubeva, E., Jackson, J. M., Krishfield, R., McCall, M., et al. (2014). Mechanisms of Pacific Summer water variability in the Arctic's Central Canada Basin. *Journal of Geophysical Research: Oceans*, *119*, 7523–7548. https://doi.org/10.1002/2014JC010273

Wang, X., Zhao, J., Lobanov, V. B., Kaplunenko, D., Rudykh, Y. N., He, Y., & Chen, X. (2021). Distribution and transport of water masses in the East Siberian Sea and their impacts on the Arctic halocline. *Journal of Geophysical Research: Oceans*, *126*, e2020JC016523. https://doi.org/10.1029/2020JC016523

Woodgate, R. A. (2018). Increases in the Pacific inflow to the Arctic from 1990 to 2015, and insights into seasonal trends and driving mechanisms from year-round Bering Strait mooring data. *Progress in Oceanography*, *160*, 124–154. https://doi.org/10.1016/j.pocean.2017.12.007

Woodgate, R. A., Aagaard, K., Swift, J. H., Falkner, K. K., & Smethie, W. M. (2005). Pacific ventilation of the Arctic Ocean's lower halocline by upwelling and diapycnal mixing over the continental margin. *Geophysical Research Letters*, *32*, L18609. https://doi.org/10.1029/2005GL023999

Woodgate, R. A., & Peralta-Ferriz, C. (2021). Warming and freshening of the Pacific inflow to the Arctic from 1990-2019 implying dramatic shoaling in Pacific winter water ventilation of the Arctic water column. *Geophysical Research Letters*, *48*, e2021GL092528. https://doi.org/10.1029/2021GL092528